UNIVERSITÄTSKLINIKUM HAMBURG-EPPENDORF

Klinik und Poliklinik für Neurologie
Prof. Dr. med. Tim Magnus

Characterization of the meningeal immune compartment in ischemic stroke employing a single-cell atlas and flow cytometry of dural immune cells

Dissertation

zur Erlangung des Grades eines Doktors der Medizin
an der Medizinischen Fakultät der Universität Hamburg.

vorgelegt von:

Mingming Zha
aus Henan, China

Hamburg 2023

(wird von der Medizinischen Fakultät ausgefüllt)

Angenommen von der
Medizinischen Fakultät am: 27.02.2024

Veröffentlicht mit Genehmigung der
Medizinischen Fakultät der Universität Hamburg.

Prüfungsausschuss, der/die Vorsitzende: Prof. Dr. Hans-Willi Mittrücker

Prüfungsausschuss, zweite/r Gutachter/in: PD Dr. Mathias Gelderblom

Content

1. Aims of the study

Meninges not only cover and protect the brain from pathogens invasion but also produce cytokines that modulate behaviors (Alves de Lima et al. 2020, Filiano et al. 2016, Mollgard et al. 2023). Multiple immune cells reside in different layers of the meninges (Mrdjen et al. 2018, Van Hove et al. 2019). The dura, the outer layer of the meninges, connects to the skull and has a complex immune landscape (Kolabas et al. 2023, Mundt et al. 2022). Dural sinuses are immune hubs facilitating immune surveillance (Rustenhoven et al. 2021). To date, multiple studies have adopted single-cell RNA sequencing (scRNAseq) to explore immune cells in the dura under different states. Nonetheless, the restricted cell numbers and the heterogeneity among the studies impede a comprehensive understanding of the dural immune compartment.

Acute ischemic stroke (AIS) is one of the leading causes of death and disability worldwide (G. B. D. Stroke Collaborators 2019). After AIS onset, peripheral immune cells including interleukin-17-producing γδ T cells (IL-17$^+$ γδ T cells) infiltrate into the brain and exacerbate tissue damage (Akopov et al. 1996, Gelderblom et al. 2009, Shichita et al. 2009). Apart from the brain, immune cell migration and activation might also happen in meninges after AIS. IL-17$^+$ γδ T cells might migrate from intestine to the meninges and modulate ischemic injury after AIS (Benakis et al. 2016). AIS might trigger the release of neutrophils from the skull bone marrow, and these neutrophils might migrate towards the dura (Herisson et al. 2018, Kolabas et al. 2023). However, the impact of AIS on the dural immune compartment is still uncertain. Furthermore, the roles of γδ T cells in the dura following AIS remain ambiguous.

The aims of this study are as follows: (i) to investigate the differences in the composition of dural immune cells under various pathological conditions and in aging; (ii) to analyze the influence of AIS on the dural immune compartment; and (iii) to explore the functions of dural γδ T cells and their impact on the dural immune landscape following AIS.

2. Introduction

2.1 Understandings of meninges are still evolving

Meninges are three-layer tissues that cover the brain and connect to the skull, which consist of dura, arachnoid, and pia (Coles et al. 2017). In the past, the meninges were mainly recognized as border tissues that separate the brain from the periphery. In 2015, functional lymphatic vessels adjacent to the dura sinuses have been found (Louveau et al. 2015). In recent years, the structures and functions of meninges have emerged as research hotspots (Kolabas et al. 2023, Mollgard et al. 2023, Rustenhoven et al. 2021), and understandings of meninges are continually evolving.

2.2 Immune cells residing in the meninges also modulate neurological functions

Meningeal immune cells not only participate in immune surveillance. T cells residing in the meninges can also modulate neuronal functions. IL-4 and IL-13 produced by meningeal T cells can regulate learning and memory (Brombacher et al. 2017, Derecki et al. 2010). Meninges-derived interferon-gamma (IFN-γ) influences neuronal connectivity and social behaviors (Filiano et al. 2016). Depleting meningeal γδ T cells leads to fewer anxiety behaviors compared with wild-type controls (Alves de Lima et al. 2020). Besides, IL-17$^+$ γδ T cells in the meninges can modulate synaptic plasticity and short-term memory (Ribeiro et al. 2019). These data suggest that the meninges not only function as immunological barriers but also have unique physiological effects on the brain parenchyma in homeostasis.

2.3 Dura has a complex immune landscape and acts as an important niche between the periphery and central nervous system (CNS)

As the outer layer of the meninges, the dura attaches to the skull directly and has the most complex immune cell landscape compared to the other two layers of meninges (Mundt et al. 2022). A scRNAseq study has revealed that multiple immune cells reside in the dura, including T cells, B cells, neutrophils, macrophages, subtypes of dendritic cells (DC), and

different kinds of monocytes (Van Hove et al. 2019). The dural sinuses are immune hubs facilitating immune surveillance (Rustenhoven et al. 2021). Moreover, connections between the dura and skull bone marrow have also been described in multiple studies (Cai et al. 2019, Herisson et al. 2018, Mazzitelli et al. 2022, Pulous et al. 2022). Under pathological conditions including stroke (Kolabas et al. 2023) and meningitis (Herisson et al. 2018), inflammatory cells might migrate from the skull bone marrow to the dura. Besides, γδ T cells might also migrate from the dura to the brain parenchyma after cerebral microbleeds (Su et al. 2023). These data suggest that the dura has a complex immune landscape, and interactions among immune cells may be prevalent among the skull bone marrow, dura, and brain parenchyma.

To date, numerous studies have explored changes of dural immune cells on single-cell level, involving aging, photothrombotic injury (PT), traumatic brain injury (TBI), experimental autoimmune encephalomyelitis (EAE), and temporary middle cerebral artery occlusion (tMCAO) models (Beuker et al. 2022, Bolte et al. 2023, Brioschi et al. 2021, Koh et al. 2020, Li et al. 2022, Li et al. 2023, Niu et al. 2022, Pinho-Ribeiro et al. 2023, Rebejac et al. 2022, Rustenhoven et al. 2021, Schafflick et al. 2021, Van Hove et al. 2019). However, the limited number of cells and heterogeneities among the studies hinder a comprehensive understanding of the dural immune compartment. Integrated analyses of the available data are necessary to effectively characterize the dural immune landscape.

2.4 AIS causes high disease burdens, and immune cells infiltrate into the brain and dura after AIS

Stroke is one of the leading causes of mortality and disability worldwide (G. B. D. Stroke Collaborators 2019), and more than 60 percent of stroke patients suffer from AIS (Wang et al. 2017). In recent years, the applications of endovascular treatments and thrombolysis have significantly improved the clinical outcomes of AIS patients (Berkhemer et al. 2015, Campbell et al. 2015, Goyal et al. 2015, Jovin et al. 2015, Nogueira et al. 2018, Saver et

al. 2015, Wang et al. 2023). However, the relatively short intravenous thrombolysis time window (Powers et al. 2019), low functional independence rates even after successful recanalization (Yeo et al. 2019), and high complication rates (He et al. 2022) advocating for advancements in innovative drugs, devices, and a deeper understanding of stroke mechanisms.

Following the onset of AIS, the deprivation of oxygen and glucose leads to cellular death, the release of damage-associated molecular patterns (Shichita et al. 2017), and the disruption of the blood-brain barrier, enabling peripheral immune cells to penetrate the brain. A previous study has demonstrated that peripheral immune cells, including neutrophils, DCs, and macrophages, infiltrate the brain after the onset of AIS (Gelderblom et al. 2009). Moreover, the gathering of polymorphonuclear leukocytes in the infarction zone is associated with brain tissue damage (Akopov et al. 1996). Myeloid cells might migrate from the bone marrow to the dura in the AIS disease model (Herisson et al. 2018, Kolabas et al. 2023), but the impact of this phenomenon on the ischemic brain remains unknown. In conclusion, these data indicate that brain-infiltrating immune cells are abundant following the onset of AIS and may have an impact on AIS outcomes. The immune landscape of the dura appears to be influenced by AIS and still requires further exploration.

2.5 Roles of dural γδ T cells after AIS are still unclear

After AIS, brain infiltrating IL-17$^+$ γδ T cells could amplify inflammatory processes and exacerbate cerebral damage (Shichita et al. 2009). Neutralization of IL-17A within three hours after AIS leads to a lower mortality rate and smaller infarction size (Gelderblom et al. 2023). A previous study has discovered that IL-17$^+$ γδ T cells could migrate from the intestine to the meninges and modulate ischemic injury following AIS (Benakis et al. 2016). Of note, γδ T cells are enriched in barrier tissues including meninges already under baseline conditions (Ribot et al. 2021). Furthermore, IL-17A$^+$ γδ T cells are also present in the meninges in homeostasis (Alves de Lima et al. 2020). More γδ T cells have been

observed in the dura compared to the pia (Beuker et al. 2022). Nevertheless, the functions of dural γδ T cells following AIS remain unclear. To sum up, these data indicate that IL-17^+ γδ T cells could be significant targets for intervention after AIS and meningeal γδ T cells may play unique roles in AIS. Investigating the alterations in dural γδ T cells following the initiation of AIS could improve the understanding of stroke mechanisms.

Taken together, the dura serves as a significant immune niche adjacent to the CNS. Nonetheless, the variations in the dural immune landscape under different conditions remain unclear. It is still uncertain whether the ischemic brain parenchyma will affect the dural immune compartment. Additionally, the functions of dural γδ T cells after AIS are still unknown. To address these questions, this study will analyze the dural immune compartment under various conditions by establishing a dural scRNAseq atlas. This study will also examine changes in dural immune cells induced by AIS using integrated scRNAseq and flow cytometric data. Furthermore, this study will investigate the impact of dural γδ T cells on the dural immune landscape after AIS through the depletion of dural γδ T cells.

3. Material and methods

3.1 The overview of this study

The general overview of this study is displayed in **Figure 1**. Two parts of scRNAseq analyses were arranged in this study. First, dural scRNAseq datasets retrieved through systematic searching before 2023-05-15 were utilized to establish a dura scRNAseq atlas and analyze the dural immune compartment under various conditions.

As for the second part, dural scRNAseq data at day 1 and day 3 after the induction of temporary middle cerebral artery occlusion (tMCAO) modeling were extracted from two studies (Beuker et al. 2022, Kolabas et al. 2023). These datasets were integrated to analyze the dural immune cell compartment and the roles of γδ T cells at different time points post-AIS.

In addition to scRNAseq analyses, flow cytometric data of the dural immune cells at baseline, day 1, and day 3 post-stroke were also collected to assess the impact of AIS on the immune landscape of the dura. Moreover, γδ T cell depletion was carried out by administering diphtheria toxin (DTX) to the Tcrd-GDL mouse line to examine the impact of γδ T cells on the dural immune compartment.

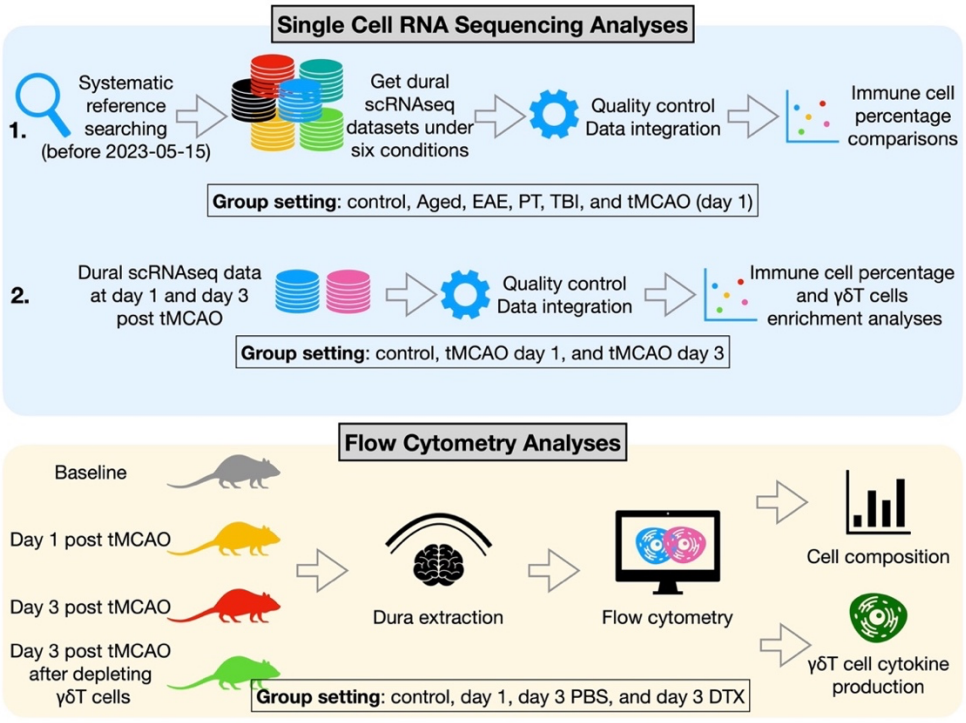

Figure 1. The schematic review of this study.

Abbreviation: scRNAseq, single cell RNA sequencing; EAE, experimental autoimmune encephalomyelitis; PT, photothrombotic injury; TBI, traumatic brain injury; tMCAO, temporary middle cerebral artery occlusion; PBS, phosphate buffered saline; DTX, diphtheria toxin.

3.2 Establishment of the dural scRNAseq atlas

3.2.1 Reference searching and data collection for the establishment of dural scRNAseq atlas

Pubmed (https://pubmed.ncbi.nlm.nih.gov/) and Gene Expression Omnibus (GEO, https://www.ncbi.nlm.nih.gov/geo/) databases were searched to retrieve all published studies that conducted scRNAseq analyses on the dura. Preferred Reporting Items for Systematic Reviews and Meta-Analyses (PRISMA) workflow was followed to ensure the correctness and completeness of reference searching (Moher et al. 2009). Medical Subject Headings (MeSH) terms and keywords were used to establish searching strategies. Detailed searching strategies of Pubmed are shown in **Table 1**.

Table 1. Searching strategies of Pubmed database.

#1	Single-Cell Gene Expression Analysis[MeSH Terms]
#2	((((((((((((((((((((((((Single Cell Transcriptome Analysis) OR (Single Cell Gene Expression Analysis)) OR (Single Cell Gene Expression Profiling)) OR (Single-Cell Gene Expression Profiling)) OR (Single-Cell Transcriptome Analysis)) OR (Analyses, Single-Cell Transcriptome)) OR (Analysis, Single-Cell Transcriptome)) OR (Single-Cell Transcriptome Analyses)) OR (Transcriptome Analyses, Single-Cell)) OR (Transcriptome Analysis, Single-Cell)) OR (Single-Cell RNA-Seq)) OR (RNA-Seq, Single-Cell)) OR (Single Cell RNA Seq)) OR (ScRNA-seq)) OR (ScRNA seq)) OR (Sc-RNAseq)) OR (Sc RNAseq)) OR (ScRNAseq)) OR (Single-Cell RNA Seq)) OR (RNA Seq, Single-Cell)) OR (Seq, Single-Cell RNA)) OR (Seqs, Single-Cell RNA)) OR (Single-Cell RNAseq)) OR (RNAseq, Single-Cell)) OR (Single Cell RNAseq)) OR (single cell RNA sequencing)) OR (single cell sequencing)
#3	#1 OR #2
#4	Meninges[MeSH Terms]

#5	Meninges
#6	Dura Mater[MeSH Terms]
#7	(((((Dura Mater) OR (Pachymeninx)) OR (Tentorium Cerebelli)) OR (Falx Cerebelli)) OR (Falx Cerebri)) OR (dura)
#8	#4 OR #5 OR #6 OR #7
#9	#3 AND #8

Abbreviation: MeSH, Medical Subject Headings; scRNAseq, single-cell RNA sequencing.

Reference searching was finished between 2023-05-13 and 2023-05-15, and 301 and 202 items were retrieved from Pubmed and GEO, respectively. Searching records were filtered by reading abstracts and full text. Inclusion criteria were: (1) Mouse related studies; (2) scRNAseq studies with complete dura immune cell populations (all $Cd45^+$ cells sorted by fluorescence-activated cell sorting machine with/without proportionally adding $Cd45^-$ cells or whole dura scRNAseq); (3) More than 200 immune cells after demultiplexing.

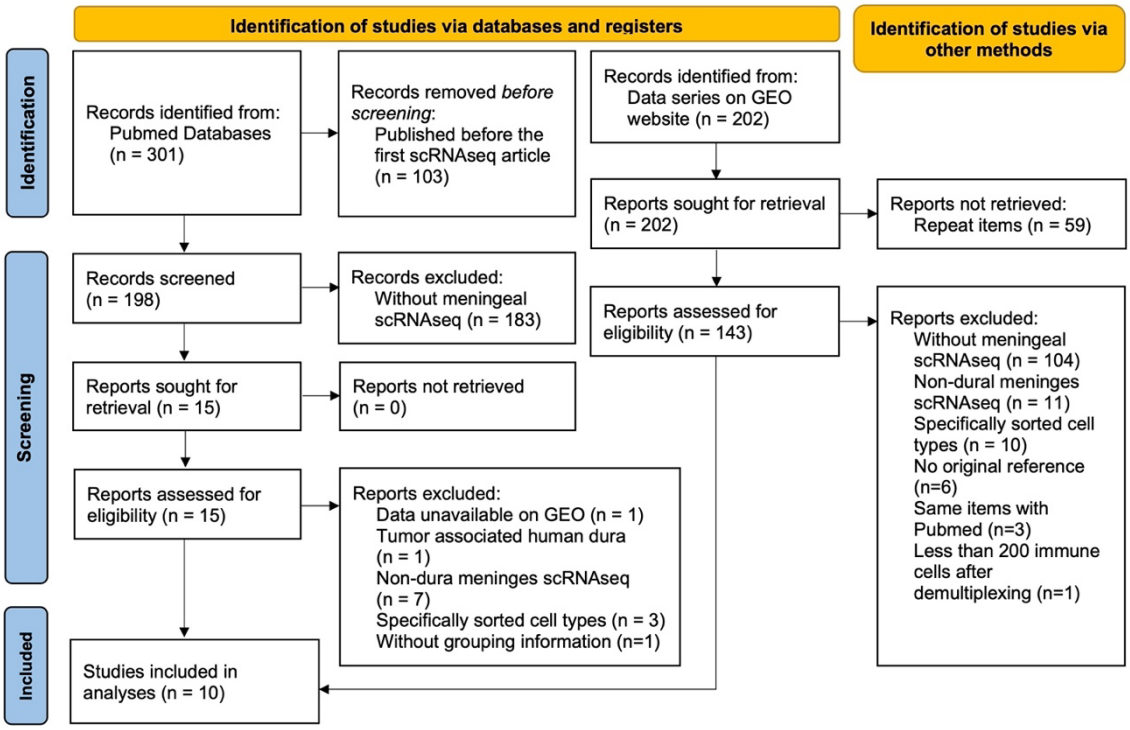

Figure 2. The PRISMA flow diagram of this study.
Abbreviations: scRNAseq, single-cell RNA sequencing; GEO, Gene Expression Omnibus; PRISMA, Preferred Reporting Items for Systematic Reviews and Meta-Analyses.

After analyzing the search results, gene expression matrices, barcodes, and unique molecular identifier information were downloaded from the GEO database. Details including author information, mouse type, age, group settings, and other relevant data were collected from the full text of references. The PRISMA flow diagram is presented in **Figure 2**. Ultimately, 10 studies that met the inclusion criteria were utilized to create the integrated scRNAseq atlas (Beuker et al. 2022, Bolte et al. 2023, Brioschi et al. 2021, Koh et al. 2020, Li et al. 2023, Niu et al. 2022, Pinho-Ribeiro et al. 2023, Rustenhoven et al. 2021, Schafflick et al. 2021, Van Hove et al. 2019).

3.2.2 Analyses of the scRNAseq atlas

All analyses of the scRNAseq data were performed on R version 4.3.1 (R Core Team 2023). The Seurat R package v4 (Hao et al. 2021) was used to process the gene expression data from each study. Ambient RNA from each sample was removed by applying the DecontX R package official workflow (Yang et al. 2020). All samples were merged into one Seurat object, and low-quality cells were filtered. A previous study has shown that neutrophils have very low transcript counts (Zilionis et al. 2019), so cell filtering thresholds were set as (nCount_RNA>500 & nCount_RNA<15000 & nFeature_RNA>100 & nFeature_RNA<4700 & percentage of mitochondria genes<10). After filtering, the Seurat object was separated by sample, and doublets in each sample were distinguished by the DoubletFinder R package (McGinnis et al. 2019), and purified datasets were merged again with the scCustomize R package (Marsh et al. 2023). Then mitochondria and ribosome structure genes were removed from the gene expression matrix (Xue et al. 2022). The merged Seurat object was normalized and the top 2000 highly variable genes were identified. Mouse cell cycle genes were retrieved from a website (https://raw.githubusercontent.com/hbc/tinyatlas/master/cell_cycle/). Cell cycle scores (S.Score and G2M.Score) were calculated with the 'CellCycleScoring' function in the Seurat package. Gene expression data was scaled with nCount_RNA, nFeature_RNA, tissue dissociation-related genes (van den Brink et al. 2017), S.Score, and G2M.Score

before clustering to reduce potential heterogeneities.

The 'ElbowPlot' function from the Seurat package was employed to analyze the number of principal components that accounted for the highest variance, and the top 20 principal components were selected for subsequent analyses. The harmony R package was utilized to integrate different samples following official tutorials (Korsunsky et al. 2019). After integration, the 'RunUMAP, 'FindNeighbors', and 'FindClusters' functions of the Seurat were executed. The resolution of 'FindClusters' was set to 4.0 to separate the clusters well. Following clustering, cell types were determined by examining the expression levels and proportions of canonical markers obtained from published literature (Brioschi et al. 2021, Munro et al. 2022, Rustenhoven et al. 2021, Tan et al. 2019, Van Hove et al. 2019). Cells that expressed exclusive markers from different cell types were classified as doublets (Ratz et al. 2022). The SingleR R Package was also employed to predict cell annotations (Aran et al. 2019). Non-immune cells and low-quality cells (unknown and doublets) were removed before downstream analyses, and the percentages of various immune cell types were calculated for each group (control, aged, EAE, PT, TBI, and tMCAO) and each individual scRNAseq sample.

3.3 Integration of dural scRNAseq data at day 1 and day 3 post-tMCAO modeling

To characterize the impact of AIS on the dural immune landscape, scRNAseq data of dura at day 1 (Beuker et al. 2022) and day 3 post-tMCAO modeling (Kolabas et al. 2023) were integrated. Three groups (control, tMCAO day 1, and tMCAO day 3) were established, and a total of 6 scRNAseq samples of the dura were integrated (From Beuker et al. 2022: 1 sample of day 1 post-tMCAO and 1 sham control; From Kolabas et al. 2023: 2 samples of day 3 post-tMCAO, 1 naïve control, and 1 sham control). These samples were processed following the previously mentioned data processing workflow with minor adjustments. In short, low-quality cells of these samples were removed (same filtering criteria as **Method part 3.2.2**). After doublet exclusion, these samples were integrated with the harmony R package. The top 15 principal components were used for subsequent

analyses and the resolution of cell clustering was set to 2. After clustering, canonical markers were used to label the cells. Non-immune cells and low-quality cells (unknown and doublets) were removed before downstream analyses.

The percentages of various immune cell types were calculated for each scRNAseq sample. γδ17 signature scores were calculated for all γδ T cells by using the 'AddModuleScore' function in the Seurat (Tirosh et al. 2016). γδ17 signature includes *Cd44, Il23r, Ccr2, Rora, Il7r, Il2ra, Sox13, Ccr6, Rorc, Il17a, S100a6, Il18r1, Icos, Blk, Maf,* and *Cxcr6* (Tan et al. 2019), which are known markers of IL-17$^+$ γδ T cells. The 'AddModuleScore' function calculates the average expression of γδ17 signature per cell and subtracts it from the average expression of randomly selected control features (Baldominos et al. 2022). A higher γδ17 signature score for a sample suggests that the marker genes of IL-17$^+$ γδ T cells are relatively upregulated in that sample. After calculation, the Dunn Kruskal-Wallis multiple comparison test from the FSA R package (Ogle et al. 2023) was used to compare γδ17 signature scores among γδ T cells in the control, tMCAO day 1, and tMCAO day 3 groups.

Gene set enrichment analyses (GSEA) was used to compare changes in pathways between two different conditions (Subramanian et al. 2005). The biological process database in the Gene Ontology database was used as a reference (Ashburner et al. 2000, Gene Ontology Consortium et al. 2023). The 'gseGO' function in the ClusterProfile R package (Wu et al. 2021) was used to conduct GSEA on γδ T cells for comparisons between the tMCAO day 1 group and the control group, the tMCAO day 3 group and the control group, as well as the tMCAO day 3 group and the tCMAO day 1 group, respectively. Detailed parameters of the 'gseGO' function were (OrgDb= org.Mm.eg.db, ont = 'BP', minGSSize = 100, maxGSSize = 500). A positive net enrichment score (NES) in the output of GSEA indicates the upregulation of a specific pathway, while a negative NES indicates the downregulation of a specific pathway. Visualizations of GSEA results were generated using the Gseavis R package (Zhang 2022).

3.4 Flow cytometric experiments

3.4.1 Guideline and animal protocol

Animal experiments were performed following regulations of the national and animal facility of the University Medical Center Hamburg-Eppendorf (UKE). All experiments on the animals were approved by the local animal care committee (Behörde für Lebensmittelsicherheit und Veterinärwesen, project number: TVA 79/19, TVA 29/21, ORG_983, and ORG_1123).

3.4.2 Mouse line information

Tcrd-GDL mouse line was used in this study. The characteristics of this mouse line have been thoroughly described in a previous publication (Sandrock et al. 2018). In general, these mice express enhanced green fluorescent protein (eGFP), human diphtheria toxin (DTX) receptor, and luciferase under the control of an internal ribosome entry site in the 3'UTR of the *Tcrd* constant gene. Cytoplasmic eGFP expression signal can be used to discriminate γδ T cells specifically. After injecting DTX intraperitoneally, γδ T cells can be effectively depleted (Sandrock et al. 2018).

3.4.3 Group setting and allocation

Regarding the flow cytometric experiments, four groups were established based on the type of reagent injection and the timing of experiments after tMCAO modeling: the control group (naïve control, mice without any intervention), day 1 group (day 1 post-tMCAO modeling), day 3 PBS group (day 3 post-tMCAO modeling without γδ T cell depletion), and day 3 DTX group (day 3 post-tMCAO modeling with γδ T cell depletion). The detailed timelines for all groups are presented in **Figure 3**.

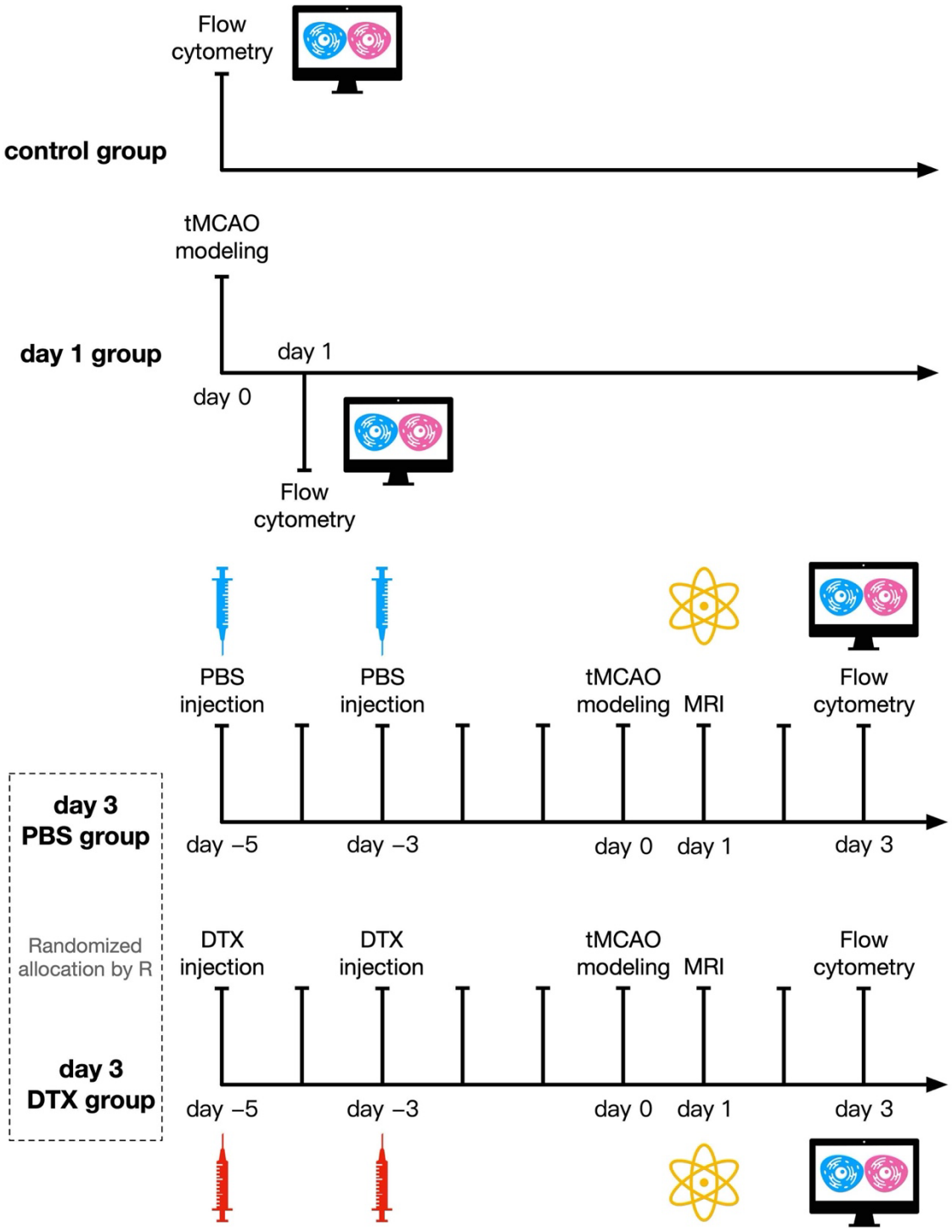

Figure 3. The group configurations and schedules of flow cytometric experiments. Abbreviations: tMCAO, temporary middle cerebral artery occlusion; PBS, phosphate buffered saline; MRI, Magnetic resonance imaging; DTX, diphtheria toxin.

Mice were randomly allocated to either the day 3 PBS or day 3 DTX group using R software (R Core Team 2023). The flow diagram of the day 3 PBS and day 3 DTX groups

is illustrated in **Figure 4**. The dose for DTX injection was calculated based on mouse weight (15 ng/g), and 200 μl of diluted DTX solution or PBS was administered intraperitoneally as the planned schedule. After injection, the mice were checked daily before tMCAO modeling. The alterations in spontaneous behaviors and facial expressions were recorded.

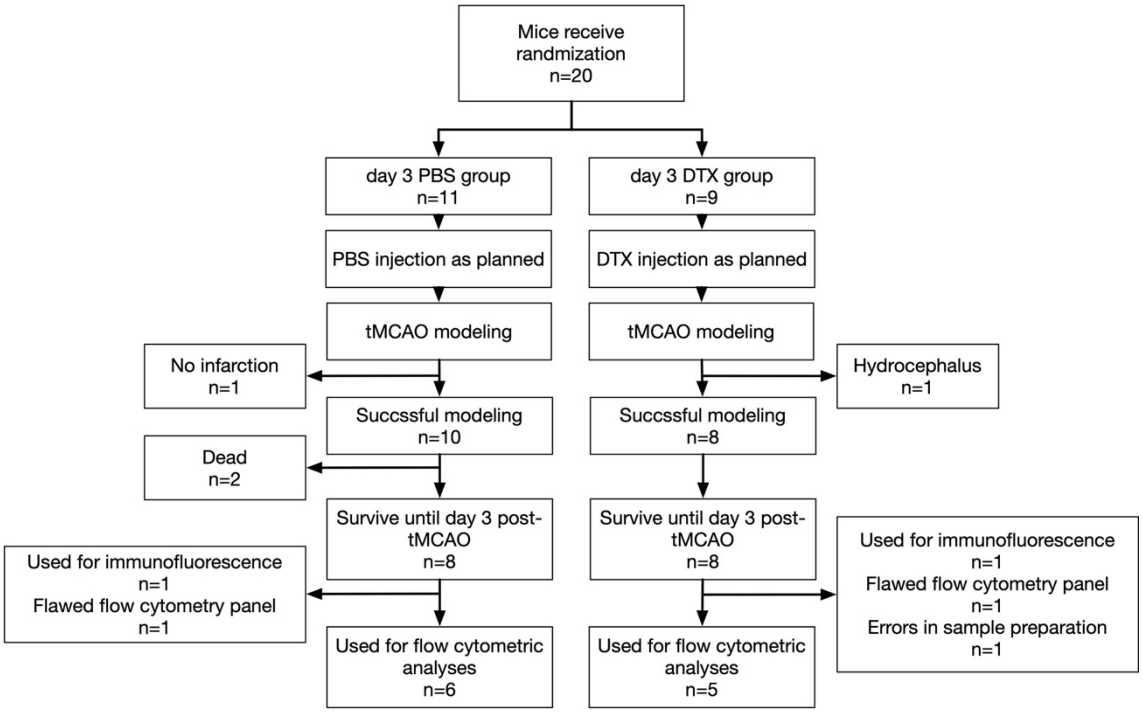

Figure 4. The flow diagram of the day 3 PBS and day 3 DTX groups.
Abbreviations: PBS, phosphate buffered saline; DTX, diphtheria toxin; tMCAO, temporary middle cerebral artery occlusion.

The age range of all mice was 10-16 weeks. To increase the persuasiveness and generalizability of the results, both genders were used. Distributions of male and female mice were similar among all groups (3 male and 3 female mice in the control group; 2 male and 4 female mice in the day 1 group; 2 male and 4 female mice in the day 3 PBS group; 2 male and 3 female mice in the day 3 DTX group).

3.4.4 TMCAO stroke modeling

TMCAO stroke modeling was conducted by experienced technicians who were blinded to group allocation, and detailed modeling methods were described in previous

publications (Gelderblom et al. 2023, Gelderblom et al. 2012) with minor changes. In short, the mice were anesthetized with Isofluran (1% to 2% v/v oxygen). Buprenorphine (0.03 mg/kg body weight) was injected intraperitoneally for analgesia. An intraluminal filament was inserted into the left MCA for 45 minutes and then removed to achieve reperfusion. After modeling, mice were placed on a heated pad (37 degrees) with facilitated access to wet food and water. Experienced caregivers visited and attended to these mice at least twice a day. The alterations in weight, spontaneous behaviors, and facial expressions were recorded.

In the day 1 group, successful infarction was confirmed by observing stroke-related behaviors (Bieber et al. 2019) and visually inspecting infarction zones during the flow cytometry experiments. For the day 3 PBS and day 3 DTX groups, successful infarction was determined using animal magnetic resonance imaging (MRI) provided by the Department of Diagnostic and Interventional Radiology and Nuclear Medicine in UKE (ClinScan, Bruker). Representative images of the MRI are shown in **Figure 5**. One mouse in the day 3 PBS group and two mice in the day 3 DTX group did not undergo the MRI examination. The confirmation of their infarction status was based on the observation of stroke-related behaviors and visual inspection of infarction zones during the flow cytometric experiments.

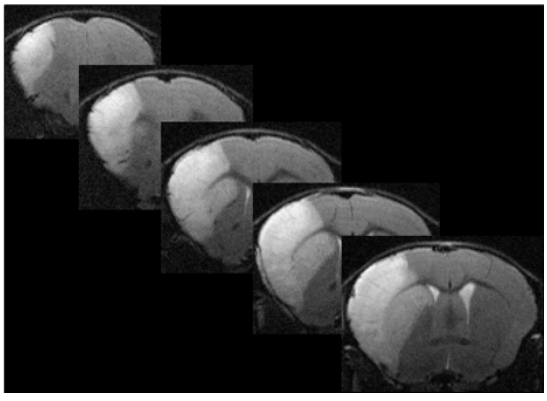

Figure 5. The representative images of brain infarction identified by MRI (representative T2 images).

3.4.5 Methodology of flow cytometry

Detailed methodologies of flow cytometry were modified based on previous publications (Derecki et al. 2010, Gelderblom et al. 2009, Scheyltjens et al. 2022). In brief, mice were killed with CO_2/O_2 and transcardially perfused with ice-cold 1x PBS for 3 minutes (9.6 ml/min). The head of mice was isolated from the thorax. Skin, muscles, eyes, and optical nerves were removed from the head. Lower jaw was removed by cutting mandibular bones at both sides. Os zygomaticus was cut from both sides, then the frontal part of nose was removed. The skull with meninges was isolated from skull base by cutting in a transverse plane at both sides. The dura was extracted from the skull under a binocular microscope (Carl Zeiss Microscopy Stand C LED, 435420-0000-000) and transferred to a 5 ml Eppendorf tube with 500 µl 4°C Dulbecco's Modified Eagle Medium (DMEM) inside. The dura was cut into pieces, and 500 µl digestion mix (DMEM + 2.0mg/ml Collagenase + 0.2 mg/ml DNAse) was added to the Eppendorf tube. Then the tube was placed into the water bath (Grant, GLS400) with agitation (15 min, 37°C). After digestion, 2 ml DMEM + 10% fetal bovine serum (FBS) was added into the Eppendorf tube to stop the enzyme reactions. Digested dura solution was transferred to a 50 ml falcon through a 40 µm cell strainer, and a plunger from a 5 ml syringe was used to grind the tissue with circulating movements. DMEM + 10% FBS was used to rinse the strainer during grinding. After grinding, the cell suspension was centrifuged at 700 relative centrifugal force (rcf) for 10 minutes at 4°C and the supernatant was discarded. The left volume was measured, and 40% was transferred to a 96-well plate for the surface staining panel. The left 60% was transferred to the other 96-well plate for the T-cell stimulation panel. After transfer, dural cells were washed twice with ice-cold 1x PBS.

For the surface staining panel, cells were incubated with a Zombie Red™ live dead staining kit (1:500 in 1x PBS) for 15 minutes on ice to label dead cells. Then cells were washed with ice-cold FACS buffer twice (47.8 ml 1x Hanks' Balanced Salt Solution [HBSS] + 0.2 ml 0.5M Ethylenediaminetetraacetic acid [EDTA] + 2 ml FBS) to remove redundant live dead dyes. After washing, the cells were incubated with 10 µl Fc blocker

solutions (0.01mg/ml) for 10 minutes on ice before incubating with the antibodies. After blocking, antibody mix of surface staining (AF700 Ly6G, clone: RA3-6B2, dilution 1:100, BioLegend; APC CD4, clone: RM 4-5, dilution 1:100, BioLegend; PE-Cy7 CD11b, clone: M 1/70, dilution 1:150, BioLegend; PE CD3ε, clone: 145-2C11, dilution 1:150, BioLegend; Percp CD45, clone: 30-F11, dilution 1:150, BioLegend; BV785 Ly6C, clone: HK1.4, dilution 1:75, BioLegend; BV711 MHC II, clone: M5/114.15.2, dilution 1:125, BioLegend; BV570 CD8a, clone: 53-6.7, dilution 1:125, BioLegend; BV421 TCRγδ, clone: GL-3, dilution 1:100, BioLegend; BUV805 B220, clone: RA3-6B2, dilution 1:125, BD Bioscience; BUV737 NK1.1, clone: PK136, dilution 1:100, BD Bioscience; BUV563 F4/80, clone: T45-2342, dilution 1:100, BD Bioscience; BUV395 CD11c, clone: HL3, dilution 1:80, BD Horizon™) were added to each well, pipetted, and then incubated on ice in the dark for 30 minutes. Detailed gating strategies of the surface staining panel are displayed in **Figure 6**. After 30 minutes of incubation, cells were washed with FACS buffer twice and transferred to BD Trucount™ Absolute Counting Tubes before measurements.

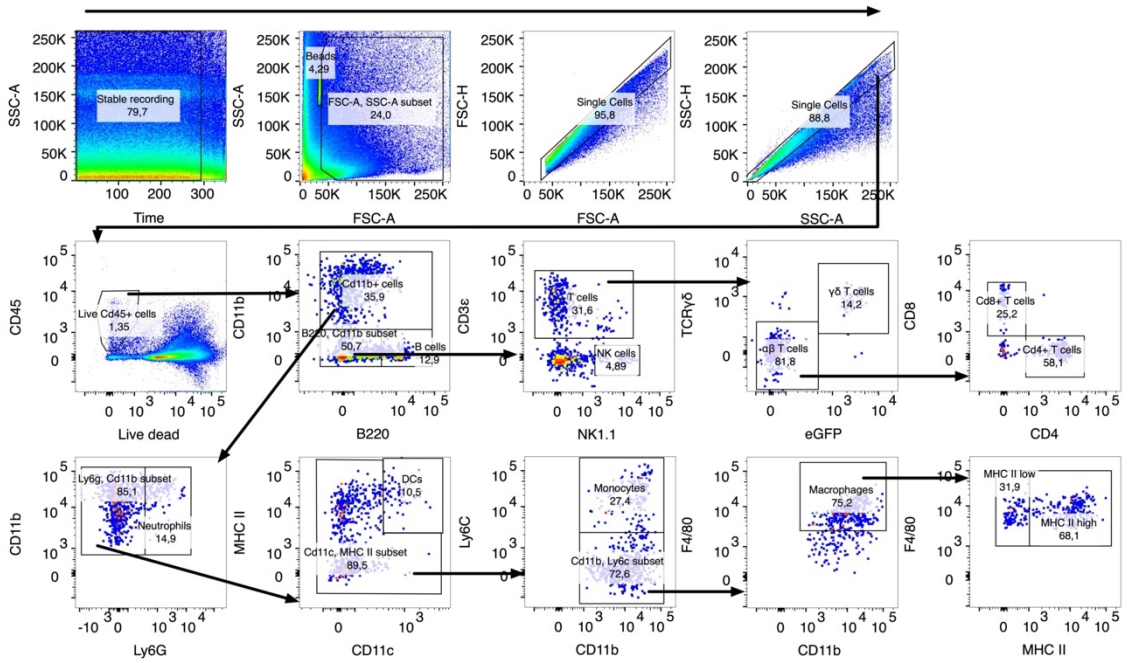

Figure 6. Illustration of the gating strategies for surface staining of dural immune cells. Stable recordings were used for downstream analyses. Debris and doublets were excluded based on the FSC and SSC parameters. The CD45 antibody and live dead marker were used together to identify

live immune cells. $CD11b^-$ and $B220^+$ cells were defined as B cells. $CD11b^+$, $B220^-$, and $Ly6G^+$ cells were defined as neutrophils. Markers of dendritic cells were $CD11b^+$, $Ly6G^-$, $CD11c^+$, and MHC II^+. The gating strategies for monocytes were defined as $CD11b^+$, $Ly6G^-$, and $Ly6C^+$. $CD11b^+$, $Ly6C^-$, and $F4/80^+$ cells were labeled as macrophages, and they were divided into MHC II high and MHC II low macrophages based on the expression levels of MHC II. $CD11b^-$, $B220^-$, $CD3^-$, and $NK1.1^+$ cells were labeled as natural killer cells. T cells ($CD11b^-$, $B220^-$, $CD3^+$) were divided into γδ T cells ($eGFP^+$ and $TCR\gamma\delta^+$) and αβ T cells ($eGFP^-$ and $TCR\gamma\delta^-$), and αβ T cells were subdivided into $CD4^+$ and $CD8^+$ T cells.
Abbreviations: FSC, forward scatter; SSC, side scatter; eGFP, enhanced green fluorescent protein; MHC, major histocompatibility complex.

For the T cell stimulation panel, the dural cells were incubated with 100 µl stimulation buffer (Roswell Park Memorial Institute 1640 Medium [RPMI] + 10% FBS + 1% Penicillin Streptomycin + 0.1% 50 µM β-Mercaptoethanol + 0.1% Brefeldin A + 0.1% Phorbol 12-Myristate 13-Acetate solution [1mg PMA to 10ml 99% ethanol] + 0.1% Ionomycin solution [1mg Ionomycin to 1ml 99% ethanol]) for 4 hours in a 37°C cell incubator (BINDER) with 5% CO_2. After that, cells were washed with ice-cold 1x PBS twice. The same workflow was executed as mentioned above until the surface staining was finished (surface staining antibodies of the T cell stimulation panel: Percp CD11b, clone: M 1/70, dilution 1:100, BioLegend; BV785 CD69, clone: H1.2F3, dilution 1:75, BioLegend; BV711 NK1.1, clone: PK 136, dilution 1:100, BioLegend; BV421 TCRγδ, clone: GL-3, dilution 1:50, BioLegend; BUV805 B220, clone: RA3-6B2, dilution 1:125, BD Bioscience; BUV737 CD3, clone: 17A2, dilution 1:100, BD Bioscience; BUV563 CD45, clone: 30-F11, dilution 1:125, BD Bioscience; BUV395 CD8a, clone: 53-6.7, dilution 1:100, BD Bioscience). Then the cells were fixed by fixation buffer for 20 minutes at room temperature. Permeabilization buffer from the same kit was diluted as recommended and used to wash the cells.

After washing, the intracellular staining antibodies mix (AF700 IFN-γ, clone: XMG 1.2, dilution 1:50, BioLegend; APC CD4, clone: RM 4-5, dilution 1:100, BioLegend; PE-Cy7 granulocyte-macrophage colony-stimulating factor (GM-CSF), clone: MP1-22E9, dilution 1:80, BioLegend; PE IL-17A, clone: eBio17B7, dilution 1:30, eBioscience) was added to the well and incubated for 20 minutes at room temperature. Detailed gating

strategies of the T cell stimulation panel are shown in **Figure 7**.

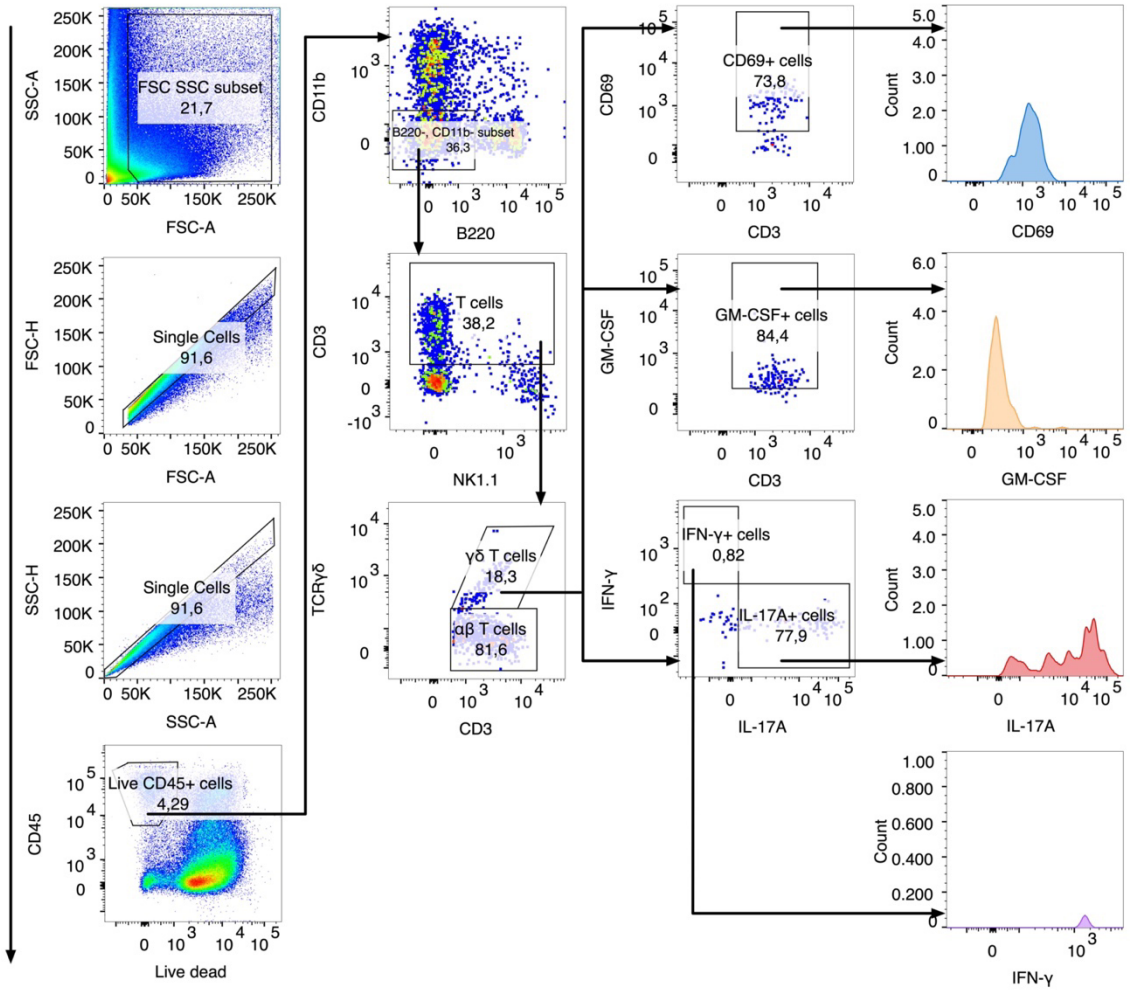

Figure 7. Illustrations of the representative staining results of dural γδ T cells in the T cell stimulation panel. The FlowAI plugin of Flowjo was used to remove low-quality events. Debris and doublets were excluded based on the FSC and SSC parameters. The CD45 antibody and live dead marker were used together to identify live immune cells. $CD45^{+}$, $CD11b^{-}$, $B220^{-}$, and $CD3^{+}$ cells were labeled as T cells. $TCR\gamma\delta^{+}$ T cells were labeled as γδ T cells. Then IL-17A, IFN-γ, GM-CSF, and CD69 antibodies were used to characterize the phenotypes of γδ T cells.
Abbreviations: FSC, forward scatter; SSC, side scatter; GM-SCF, granulocyte-macrophage colony-stimulating factor.

Thresholds for CD69, GM-CSF, IFN-γ, and IL-17A were set by the fluorescence-minus-one (FMO) controls in each experiment. The FMO controls demonstrate the fluorescent spread of CD69, GM-CSF, IFN-γ, and IL-17A in multicolor flow cytometry panels by removing one fluorophore at a time. Spleen cells from the Tcrd-GDL mice line were used

for FMO controls, and illustrations of setting gating thresholds are shown in **Figure 8**. After washing with permeabilization buffer and FACS buffer, the cells were transferred to 5 ml FACS tubes and measured using the BD FACS Symphony A3.

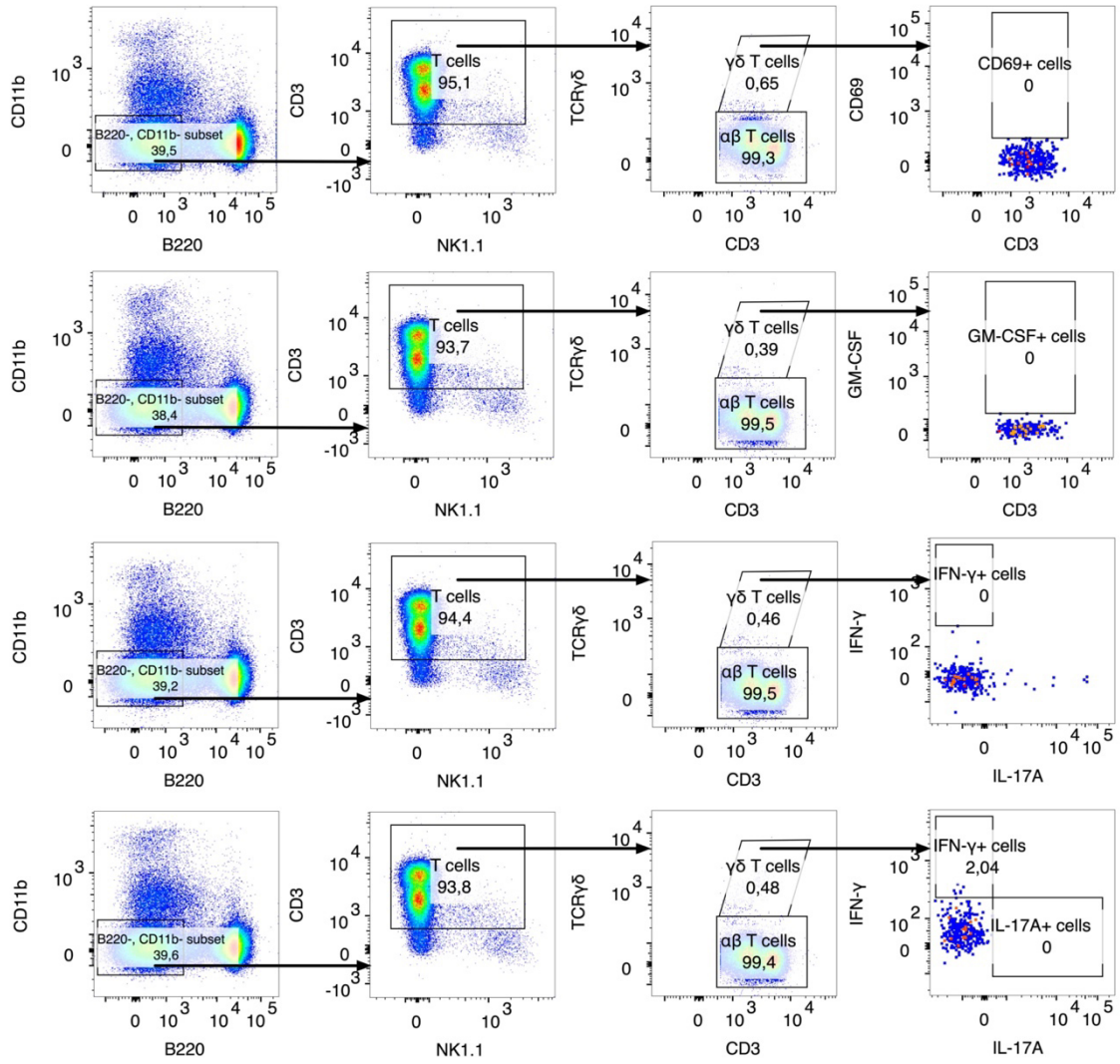

Figure 8. Illustrations of setting gating thresholds for CD69, GM-CSF, IFN-γ, and IL-17A in γδ T cells. The FlowAI plugin of Flowjo was used to remove low-quality events. Debris and doublets were excluded based on the FSC and SSC parameters. The CD45 antibody and live dead marker were used together to identify live immune cells. $CD45^{+}$, $CD11b^{-}$, $B220^{-}$, and $CD3^{+}$ cells were labeled as T cells. $TCR\gamma\delta^{+}$ T cells were labeled as γδ T cells. Spleen cells from homozygous Tcrd-GDL mice were used for the FMO controls in each flow cytometric experiment. The FMO controls demonstrate the fluorescent spread of CD69, GM-CSF, IFN-γ, and IL-17A in multicolor flow cytometry panels by removing one fluorophore at a time.

Abbreviations: FSC, forward scatter; SSC, side scatter; GM-SCF, granulocyte-macrophage colony-stimulating factor.

3.4.6 Analyses of flow cytometric data

Analyses on the flow data were performed using Flowjo software (BD, version 10.9). In samples containing TruCount™ beads, only stable recording periods were considered for further analysis. The FlowAI plugin (Monaco et al. 2016) in the Flowjo was employed to remove low-quality events from samples without TruCount™ beads before downstream analyses. For the surface staining panel, cell counts were calculated with the beads recorded in the BD FACS Symphony A3 and the original beads number included in the BD Trucount™ tube (Schnizlein-Bick et al. 2000), and the calculation formula was: (number of recorded cells) * (original beads number) / (number of recorded beads).

For γδ T cells in the T cell stimulation panel, percentages of $CD69^+$, $GM\text{-}CSF^+$, $IFN\text{-}\gamma^+$, and $IL\text{-}17A^+$ cells were calculated. The median function in Flowjo was used to calculate Median Fluorescence Intensity (MFI) values of CD69 for $CD69^+$ cells. And same procedures were performed to calculate relevant MFI values in $GM\text{-}CSF^+$ and $IL\text{-}17A^+$ γδ T cells.

Results of flow cytometry were processed by GraphPad Prism (version: 10.1.0). Normality (Shapiro-Wilk (W) test) and homogeneity of variance (Brown-Forsythe test) of the data were checked before significance analyses. For comparisons among the control, day 1, and day 3 PBS groups, the analysis of variance (ANOVA), the Brown-Forsythe and Welch ANOVA test, or the Kruskal-Wallis test with multiple comparisons test was used based on the results of normality and homogeneity of variance tests. For comparison between the day 3 PBS group and day 3 DTX group, the unpaired t-test, the unpaired t-test with Welch's correction, or the Mann-Whitney test was applied.

3.5 Reagents used in this study

All antibodies, solutions, and other materials used in this study are listed in **Table 2**.

Table 2. The list of reagents used in this study.

Name	Source	Identifier
DTX	Merck	D0564-1MG

PBS	Gibco	10010023
Isofluran	Sedaconda	7002244.00.00
Buprenovet Multidose 0.3 mg/ml	Bayer	401513.00.00
MCAO suture	Doccol	602312PK10Re
5.0 ml Eppendorf Tube	Eppendorf	0030119401
DMEM	Gibco	41965039
Collagenase type VIII	Sigma	C2139 100mg
DNAse	Merck	10104159001
HBSS	Gibco	14025092
FBS	PAN Biotech	P40-47500
15 ml Falcon	Greiner	T1943-1000EA
50 ml Falcon	Greiner	T2318-500EA
Cell strainer	Greiner	542040
2 ml Syringe	Braun	421109
Zombie Red™ Fixable Viability Kit	BioLegend	423109
96 well plate	Greiner	650185
EDTA	Sigma-Aldrich	03690-100ML
Fc blocker	BioXCell	5806/0715
RPMI	Gibco	21875-091
Penicillin Streptomycin	Gibco	15140-122
β-Mercaptoethanol	Gibco	31350-010
Brefeldin A	Invitrogen	00-450651
Ionomycin	Sigma	I0634-1MG
PMA	Sigma	P1585-1MG
AF700 Ly6G, clone: RA3-6B2	BioLegend	127622
APC CD4, clone: RM 4-5	BioLegend	100516
PE-Cy7 CD11b, clone: M 1/70	BioLegend	101216
PE CD3ε, clone: 145-2C11	BioLegend	100308
Percp CD45, clone: 30-F11	BioLegend	103130
BV785 Ly6C, clone: HK1.4	BioLegend	128041
BV711 MHC II, clone: M5/114.15.2	BioLegend	107643

BV570 CD8a, clone: 53-6.7	BioLegend	100739
BV421 TCR γδ, clone: GL-3	BioLegend	118120
BUV805 B220, clone: RA3-6B2	BD Bioscience	748867
BUV737 NK1.1, clone: PK136	BD Bioscience	741715
BUV563 F4/80, clone: T45-2342	BD Bioscience	749284
BUV395 CD11c, clone: HL3	BD Horizon™	564080
AF700 IFN-γ, clone: XMG 1.2	BioLegend	505824
PE-Cy7 GM-CSF, clone: MP1-22E9	BioLegend	505412
PE IL-17A, clone: eBio17B7	eBioscience	12-7177-81
Percp CD11b, clone: M 1/70	BioLegend	101230
BV785 CD69, clone: H1.2F3	BioLegend	104543
BV711 NK1.1, clone: PK 136	BioLegend	108745
BUV737 CD3, clone: 17A2	BD Bioscience	612803
BUV563 CD45, clone: 30-F11	BD Bioscience	612924
BUV395 CD8a, clone: 53-6.7	BD Bioscience	563786
FACS tubes	SARSTEDT	55.1579
BD Trucount™ Trucount Absolute Counting Tubes IVD	BD Bioscience	340334
True Nuclear Fix, Nuclear staining buffer kit	Biolegend	424401

4. Results

4.1 A well-integrated dural scRNAseq atlas is established

To establish a dural scRNAseq atlas, 34 scRNAseq samples from 10 studies were included for data integration following reference filtering. Detailed descriptions of all the included studies are provided in **Table 3**. All studies utilized the C57BL/6 mouse strain and employed 10x scRNAseq kits for their scRNAseq experiments. A total of six groups were involved, including control, aged (24-25 months), PT, EAE, TBI, and tMCAO (day 1 post modeling).

Table 3. Descriptions of all enrolled studies

Year	First Author	Mouse strain	Age	Sex	$CD45^+$ cell enrichment	Platform	Group of samples	scRNAseq sample number
2019	Hannah Van Hove	C57BL/6	9 weeks	Male	Yes	10x	Ctrl	3
2020	Bong Ihn Koh	C57BL/6	8 weeks	NM	Yes	10x	Ctrl, PT	2
2021	Justin Rustenhoven	C57BL/6	8 weeks-24 months	NM	No	10x	Ctrl, Aged	4
2021	David Schafflick	C57BL/6	8-14 weeks	Both	Yes	10x	Ctrl, EAE (peak stage)	2
2021	Simone Brioschi	C57BL/6	10 weeks-25 months	Female	No	10x	Ctrl, Aged	14
2022	Chunxiao Niu	C57BL/6	8-12 weeks	Both	Yes	10x	Ctrl	1
2022	Carolin Beuker	C57BL/6	10-16 week	Male	Yes	10x	Ctrl, tMCAO (day 1 post modeling)	2
2023	Ashley C Bolte	C57BL/6	8-12 week	Male	No	10x	Ctrl, TBI	2
2023	Felipe A. Pinho-Ribeiro	C57BL/6	8-14 weeks	Both	Yes	10x	Ctrl	1
2023	Zhilin Li	C57BL/6	10-13 weeks	NM	Yes (matched with $Cd31^+$ cells)	10x	Ctrl, EAE (day 10 and 14 post-injection)	3

Abbreviations: scRNAseq, single cell RNA sequencing; NM, not mentioned; PT, photothrombotic injury; EAE, experimental autoimmune encephalomyelitis; tMCAO, temporary middle cerebral artery occlusion; TBI, traumatic brain injury.

A total of 120,893 cells were clustered after filtering and automatic doublet exclusion,

and 78 clusters were defined in the integrated dataset.

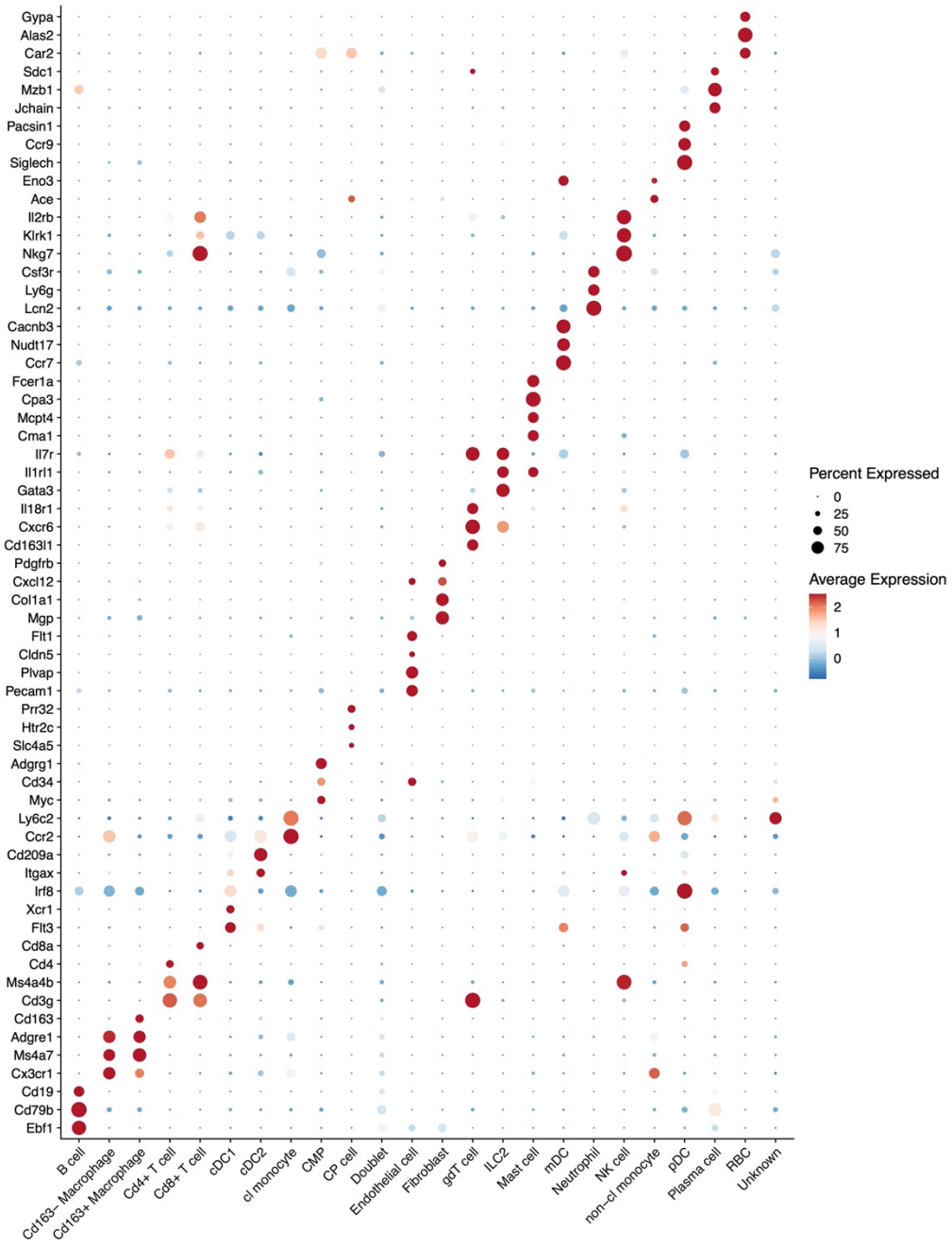

Figure 9. The canonical markers used for cell annotation in this study. The color of the dot represents scaled gene expression level, and the size of the dot represents the percentage of cells expressing these genes.

Abbreviations: cDC1, classical type 1 dendritic cell; cDC2, classical type 2 dendritic cell; cl monocyte, classical monocyte; CMP, common myeloid progenitor; CP, choroid plexus; gdT cell, γδ T cell; ILC2, group 2 innate lymphoid cell; mDC, migratory dendritic cell; NK, natural killer; non-cl monocyte, non-classical monocyte; pDC, plasmacytoid dendritic cell; RBC, red blood cell.

After checking the expression levels and percentages of canonical marker genes, B cell (*Ebf1*, *Cd79b*, and *Cd19*), Cd163^{-} macrophage (*Mrc1*, *Ms4a7* and *Adgre1*), Cd163^{+} macrophage (*Mrc1*, *Ms4a7*, *Adgre1*, and *Cd163*) , Cd4^{+} T cell (*Cd3g*, *Ms4a4b*, and *Cd4*), Cd8^{+} T cell (*Cd3g*, *Ms4a4b*, and *Cd8*), classical type 1 dendritic cell (cDC1) (*Flt3*, *Irf8*^{hi}, and *Xcr1*), classical type 2 dendritic cell (cDC2) (*Flt3*, *Irf8*^{low}, and *Cd209*), classical monocyte (*Ccr2* and *Ly6c2*), common myeloid progenitor (CMP) (*Myc*, *Cd34*, and *Adgrg1*), choroid plexus (CP) cell (*Slc4a5*, *Htr2c*, and *Prr32*), endothelial cell (*Pecam1*, *Plvap*, *Cldn5*, and *Flt1*), fibroblast (*Mgp*, *Col1a1*, *Cxcl12*, and *Pdgfrb*), γδ T cell (*Cd163l1*, *Cxcr6*, and *Il18r1*), group 2 innate lymphoid cell (ILC2) (*Gata3*, *Il1rl1*, and *Il7r*), mast cell (*Cma1*, *Mcpt4*, *Cpa3*, and *Fcer1a*), migratory dendritic cell (mDC) (*Ccr7*, *Nudt17*, and *Cacnb3*), neutrophil (*Lcn2*, *Ly6g*, and *Csf3r*), natural killer (NK) cell (*Nkg7*, *Klrk1*, and *Il2rb*), non-classical monocytes (*Ace* and *Eno3*), plasmacytoid dendritic cell (pDC) (*Siglech*, *Ccr9*, and *Pacsin1*), plasma cell (*Jchain*, *Mzb1*, and *Sdc1*), and red blood cell (*Car2*, *Alas2*, and *Gypa*) are identified in this study (**Figure 9**).

To increase the persuasiveness of cell annotations, the SingleR R package was also used to predict cell types. The automatic predictions were compared with manual annotations. The Uniform Manifold Approximation and Projection (UMAP) visualizations of predicted cell types are shown in **Figure 10**, and cell types are similar between manual annotations and SingleR predictions.

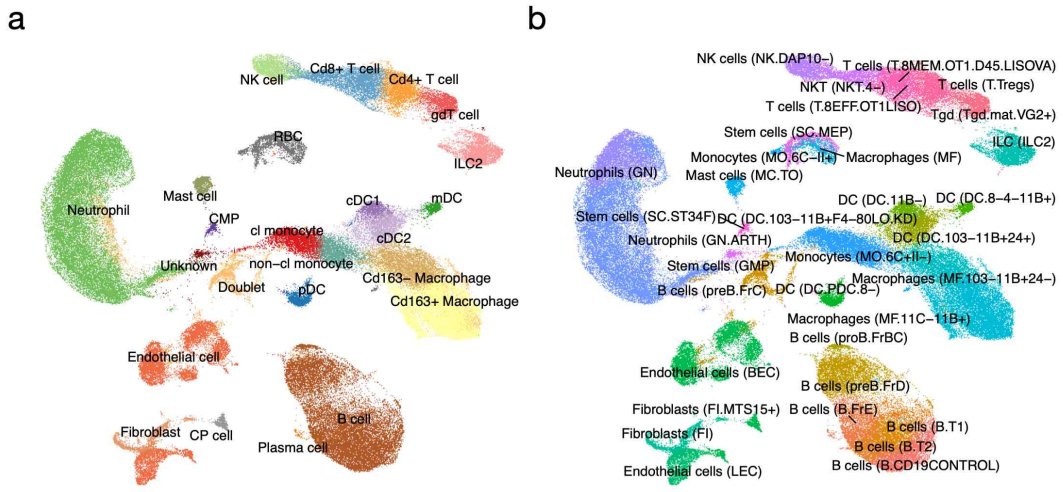

Figure 10. UMAP visualizations of predicted cell types in the integrated dural scRNAseq atlas.

All 120,893 cells from the 10 enrolled studies that fulfill the quality control standards were integrated. (a) Manual annotation with the canonical markers shown in **Figure 9**. (b) Cell labels predicted by the SingleR R package.
Abbreviations: UMAP, Uniform Manifold Approximation and Projection; scRNAseq, single cell RNA sequencing; cDC1, classical type 1 dendritic cell; cDC2, classical type 2 dendritic cell; cl monocyte, classical monocyte; CMP, common myeloid progenitor; CP, choroid plexus; gdT cell, γδ T cell; ILC2, group 2 innate lymphoid cell; mDC, migratory dendritic cell; NK, natural killer; non-cl monocyte, non-classical monocyte; pDC, plasmacytoid dendritic cell; RBC, red blood cell.

Non-immune cells were removed before downstream analyses. The UMAP visualizations of the 10 enrolled studies exhibit similar shapes, indicating that 98,195 immune cells are well-integrated in the dural scRNAseq atlas (**Figure 11**).

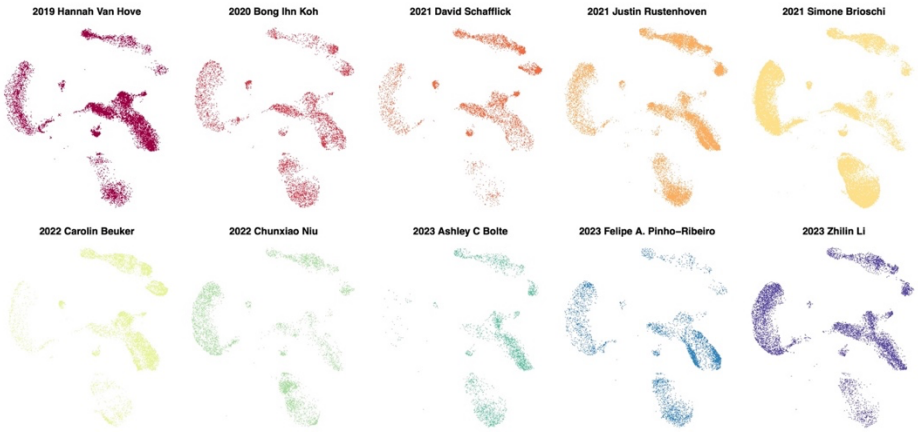

Figure 11. UMAP visualizations of the integrated dural scRNAseq atlas classified by different origins. All 98,195 immune cells from the 10 enrolled studies that fulfill the quality control standards were integrated. The publication year and name of the first author are shown above the UMAP visualization of each study.
Abbreviation: UMAP, Uniform Manifold Approximation and Projection; scRNAseq, single cell RNA sequencing.

4.2 Immune cell percentages vary among different conditions in the dural scRNAseq atlas

To investigate variations in in immune cell compositions within the dura under different conditions, the proportions of immune cells within each scRNAseq sample and each group were calculated. The aged group and EAE group have more than one scRNAseq sample, and the percentages of all immune cells were then compared between individual

samples in the aged/EAE group and the control group, respectively. Additionally, immune cell compositions across the six groups were also examined.

4.2.1 Percentages of neutrophils are higher in the aged dura

The aged group (age range: 24-25 months) has 9 biological duplicates (Brioschi et al. 2021, Rustenhoven et al. 2021), and the control group (age range: 8-16 weeks) includes 19 scRNAseq samples from the 10 enrolled studies (**Table 3**). Comparisons of the percentages of different immune cell types between the aged group and the control group are shown in **Figure 12**.

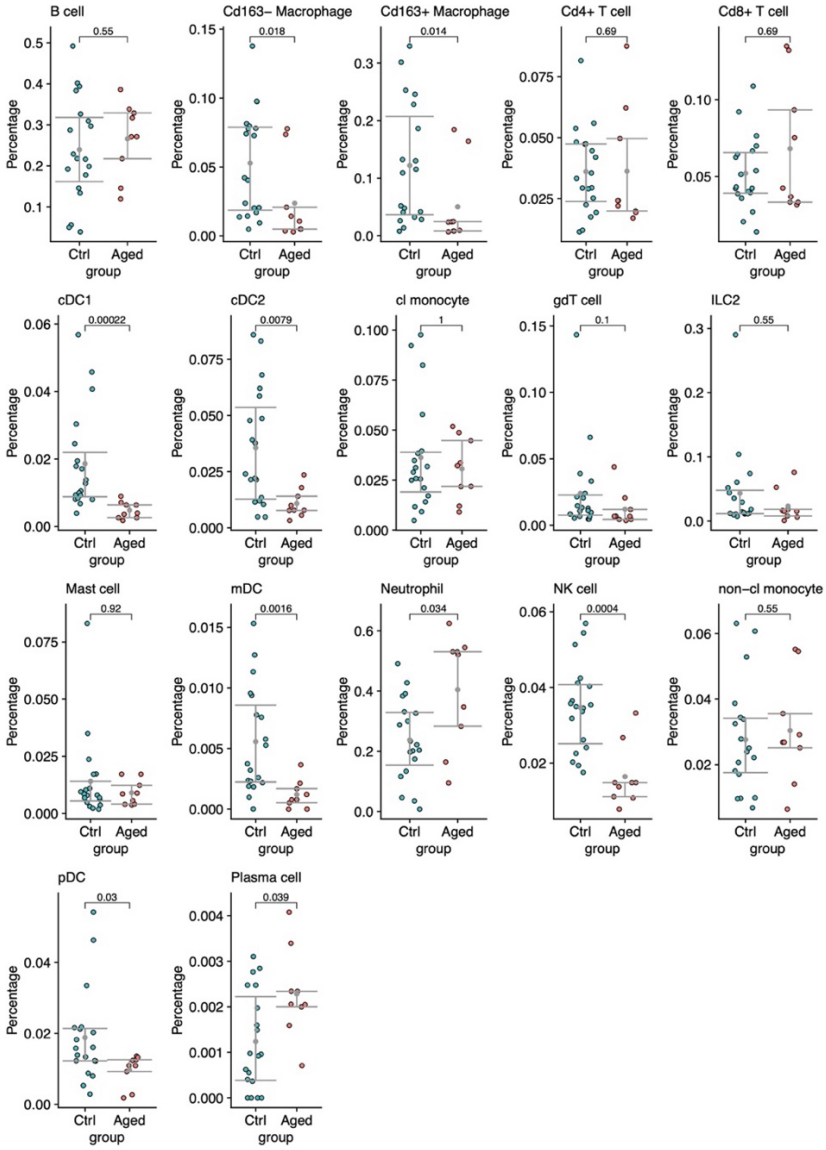

Figure 12. Immune cell percentage comparisons between the aged group and the control group.

Nine scRNAseq samples in the aged group (age range: 24-25 months) and 19 scRNAseq samples in the control group (age range: 8-16 weeks) were used. Each dot on the figure represents a scRNAseq sample. The percentage of each type of immune cell within each sample was calculated by dividing the total number of immune cells in that sample. The Wilcoxon signed-rank test was utilized to evaluate the significance of differences between the aged group and the control group for each type of immune cell.
Abbreviations: cDC1, classical type 1 dendritic cell; cDC2, classical type 2 dendritic cell; cl monocyte, classical monocyte; gdT cell, γδ T cell; ILC2, group 2 innate lymphoid cell; mDC, migratory dendritic cell; NK, natural killer; non-cl monocyte, non-classical monocyte; pDC, plasmacytoid dendritic cell.

The results indicate that the proportions of neutrophils and plasma cells in the aged group are significantly higher than those in the control group. Besides, the percentages of NK cells, subtypes of DCs (cDC1, cDC2, mDC, and pDC), and two kinds of macrophages ($Cd163^+$ macrophage and $Cd163^-$ macrophage) are significantly lower in the aged group compared to the control group.

4.2.2 Lower percentages of B cells are found in the EAE dura

Three samples are included in the EAE group, and these three samples are heterogenous regarding the sampling time (peak stage, day 10 post-injection of Myelin Oligodendrocyte Glycoprotein, and day 14 post-injection of Myelin Oligodendrocyte Glycoprotein). Therefore, the significance of difference between the EAE group and the control group (19 scRNAseq samples from the 10 enrolled studies) for each type of immune cell was not analyzed. However, according to the percentage visualizations in **Figure 13**, percentages of B cells might be lower in the EAE group compared with the control group.

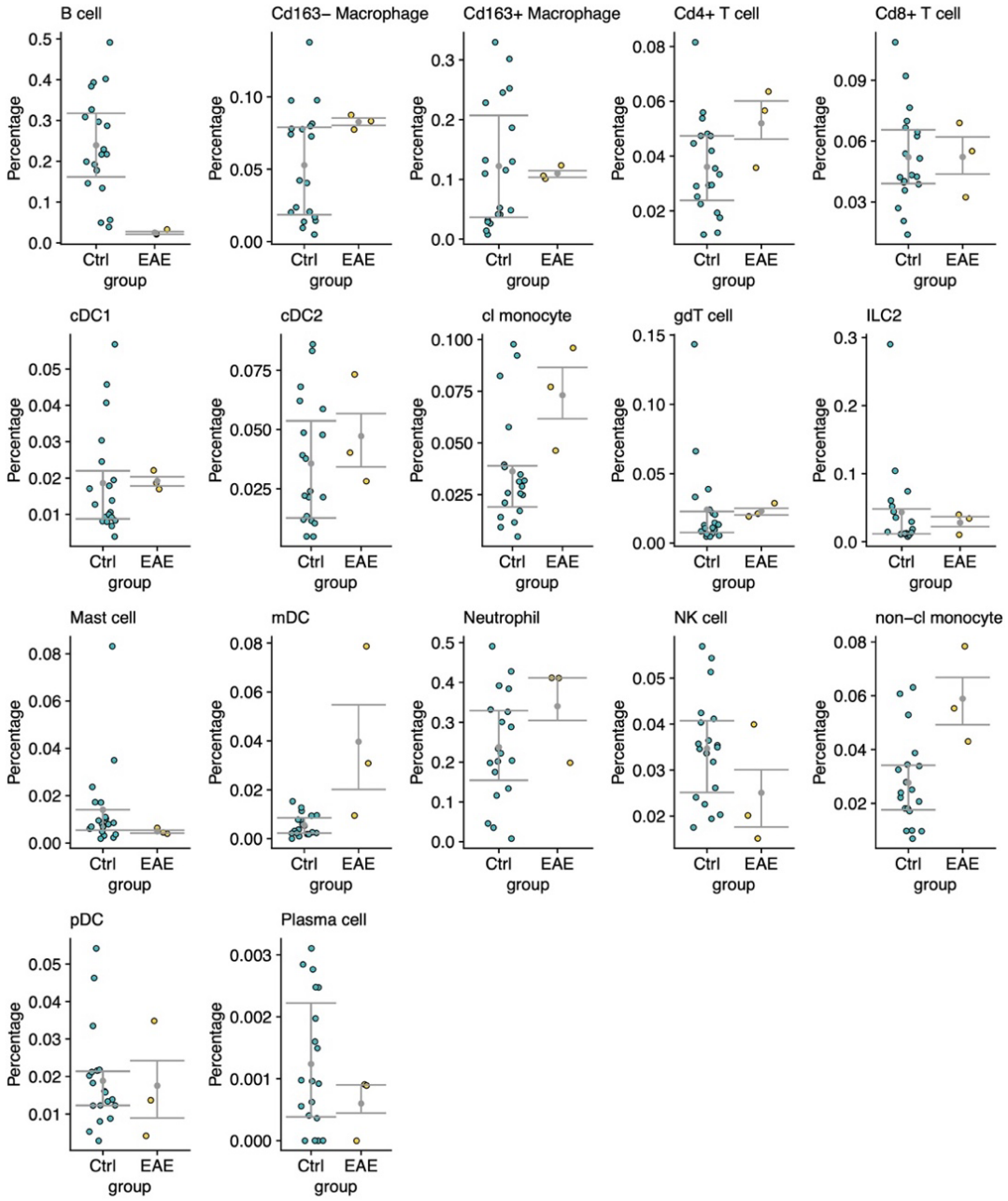

Figure 13. Immune cell percentage comparisons between the EAE group and the control group. Three scRNAseq samples in the EAE group and 19 scRNAseq samples in the control group were used. Each dot on the figure represented a scRNAseq sample, and the percentage of each type of immune cell within each sample was calculated by dividing the total number of immune cells in that sample.

Abbreviations: EAE, experimental autoimmune encephalomyelitis; cDC1, classical type 1 dendritic cell; cDC2, classical type 2 dendritic cell; cl monocyte, classical monocyte; gdT cell, γδ T cell; ILC2, group 2 innate lymphoid cell; mDC, migratory dendritic cell; NK, natural killer; non-cl monocyte, non-classical monocyte; pDC, plasmacytoid dendritic cell.

4.2.3 Proportions of immune cells in the dura are heterogeneous among different conditions

As for the PT, TBI, and tMCAO groups, all these groups have only 1 scRNAseq sample (**Table 3**). The proportions of 17 kinds of immune cells among all six groups are shown in **Figure 14**. This figure also illustrates that the immune landscapes of the dura exhibit heterogeneity under varying conditions.

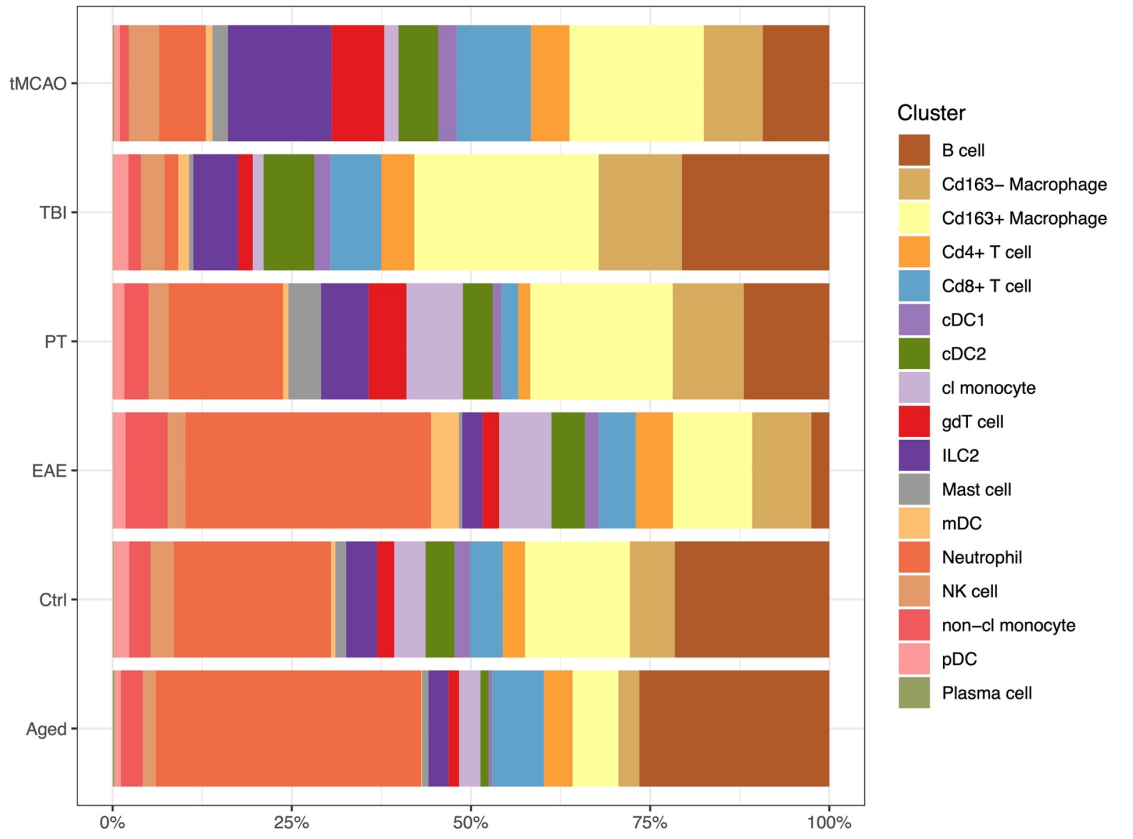

Figure 14. The proportions of all immune cells among the six groups in the dural scRNAseq atlas. All 98,195 immune cells from the integrated dural scRNAseq atlas were used. The percentage of each type of immune cell within each group was calculated by dividing the total number of immune cells in that group.

Abbreviations: tMCAO, temporary middle cerebral artery occlusion; TBI, traumatic brain injury; PT, photothrombotic injury; EAE, experimental autoimmune encephalomyelitis; cDC1, classical type 1 dendritic cell; cDC2, classical type 2 dendritic cell; cl monocyte, classical monocyte; gdT cell, γδ T cell; ILC2, group 2 innate lymphoid cell; mDC, migratory dendritic cell; NK, natural killer; non-cl monocyte, non-classical monocyte; pDC, plasmacytoid dendritic cell.

4.3 The number and percentage of dural γδ T cells seem to increase on day 1 post-tMCAO but then might relatively decrease on day 3 post-tMCAO

To explore the impact of AIS on the dural immune cells, dural scRNAseq datasets on day 1 and day 3 post-tMCAO modeling and the baseline controls from the same studies were integrated (Beuker et al. 2022, Kolabas et al. 2023). Six scRNAseq samples were used for integration (3 samples in the control group, 1 sample in the tMCAO day 1 group, and 2 samples in the tMCAO day 3 group). A total of 13 types of immune cells were identified. The UMAP visualizations of the integrated dura are shown in **Figure 15a**. As shown in **Figure 15b**, all 10,172 immune cells are well integrated among different groups.

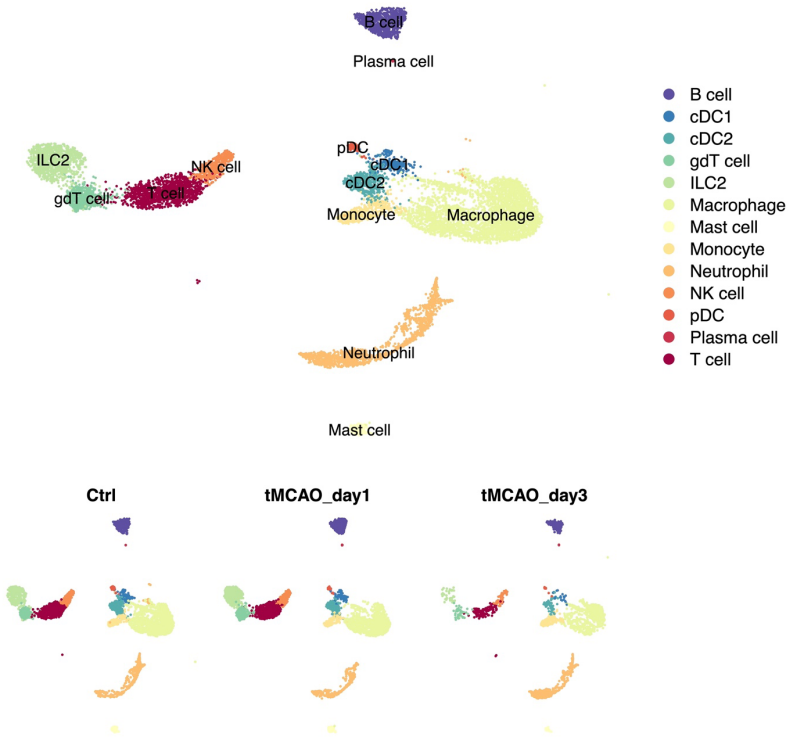

Figure 15. UMAP visualizations of various immune cell types in the integrated dural scRNAseq data. (a) UMAP visualizations of all 10,172 dural immune cells in the integrated dataset. (b) UMAP visualizations of the cells in the integrated dataset categorized by different groups. The name of each group is shown above the UMAP visualization of each study. Immune cells from two studies (Beuker et al. 2022, Kolabas et al. 2023) were integrated. Manual cell annotations were finished with the canonical markers displayed in **Figure 9**.
Abbreviations: UMAP, Uniform Manifold Approximation and Projection; scRNAseq, single cell RNA sequencing; cDC1, classical type 1 dendritic cell; cDC2, classical type 2 dendritic cell; gdT cell, γδ T cell; ILC2, group 2 innate lymphoid cell; NK, natural killer; pDC, plasmacytoid

dendritic cell; tMCAO, temporary middle cerebral artery occlusion.

The distributions of various immune cell percentages within the integrated dural scRNAseq dataset across the control group, tMCAO day 1 group, and tMCAO day 3 group are shown in **Figure 16**. The tMCAO day 1 group seems to have fewer macrophages and more T cells. The percentage of γδ T cells seems to increase in the tMCAO day 1 group compared with the control group, and then shows a decreasing trend in the tMCAO day 3 group compared with the tMCAO day 1 group.

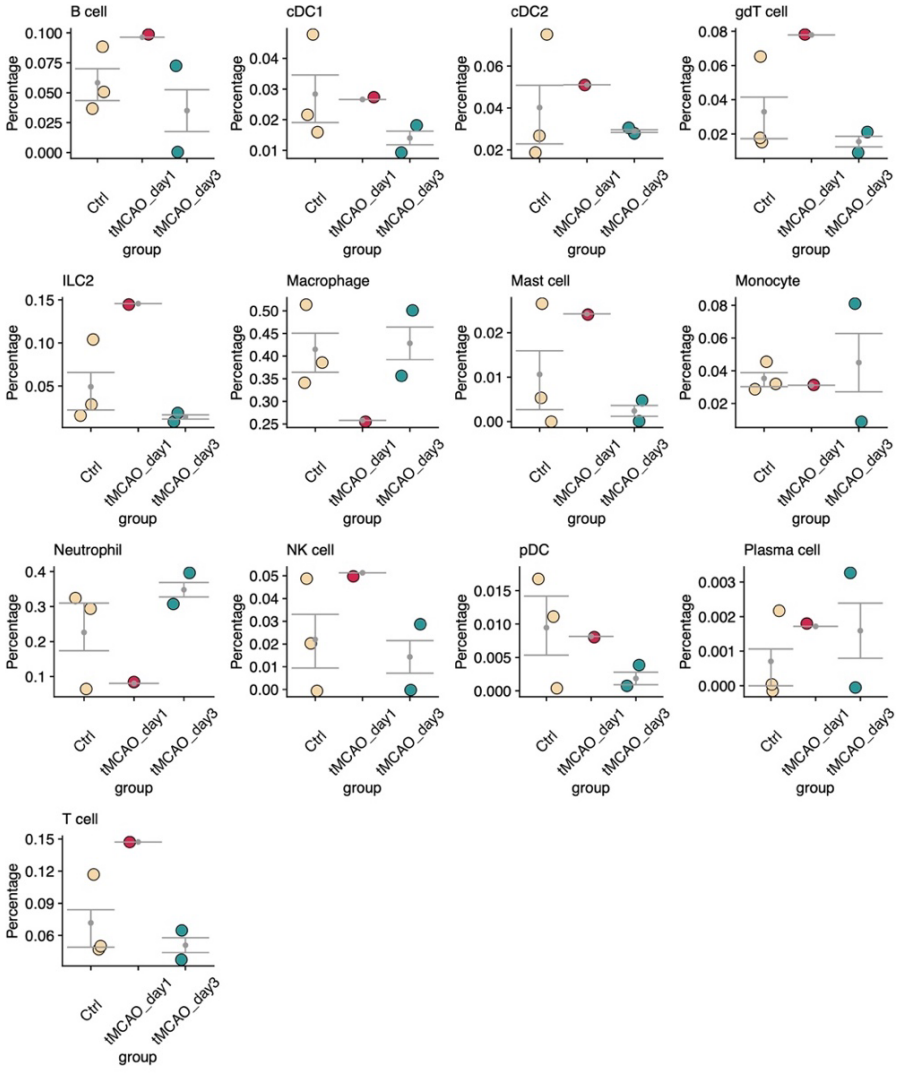

Figure 16. Immune cell percentage comparisons among the control group, the tMCAO day 1 group, and the tMCAO day 3 group in the integrated scRNAseq dataset. Three scRNAseq samples in the control group, one sample in the tMCAO day 1 group, and two samples in the tMCAO day 3 group were used. Each dot on the figure represents one scRNAseq sample. The percentage of each type of immune cell within each sample was calculated by dividing the total number of

immune cells in that sample.
Abbreviations: tMCAO, temporary middle cerebral artery occlusion; scRNAseq, single cell RNA sequencing; cDC1, classical type 1 dendritic cell; cDC2, classical type 2 dendritic cell; gdT cell, γδ T cell; ILC2, group 2 innate lymphoid cell; NK, natural killer; pDC, plasmacytoid dendritic cell.

Considering the lack of biological replicates in the integrated scRNAseq data, flow cytometric data of the control, day 1, and day 3 PBS groups were also used to analyze changes in the dural immune compartment at different time points post-AIS.

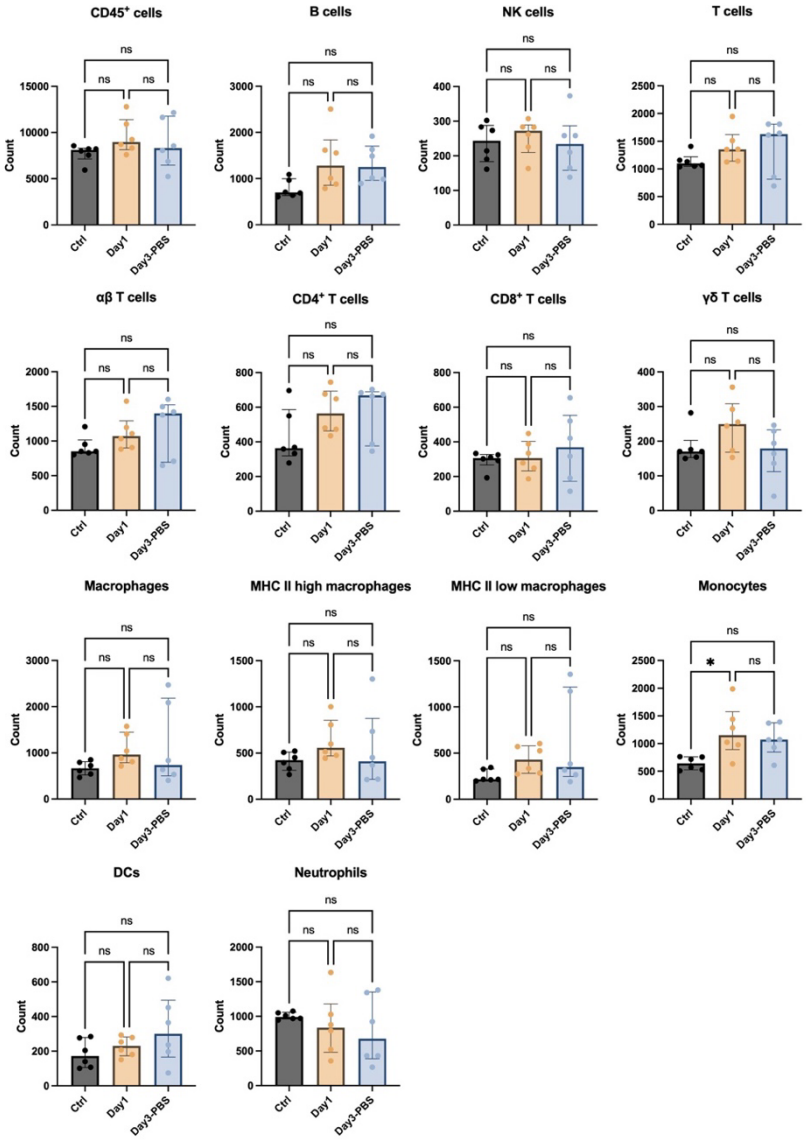

Figure 17. Comparisons on absolute numbers of different kinds of immune cells in the dura among the control, day 1, and day 3 PBS groups in the flow cytometric experiments. Data were obtained after flow cytometric analyses of dural immune cells stained for Ly6G, CD4, CD11b, CD3ε, CD45, Ly6C, MHC II, CD8a, TCRγδ, B220, NK1.1, F4/80, and CD11c. For cell counting,

BD Trucount™ Absolute Counting Tubes were used. Cell counts were calculated with the beads recorded in the BD FACS Symphony A3 and the original beads number included in the BD Trucount™ tube. Detailed gating strategies are shown in **Figure 6**. The figures show the median ± interquartile range of six Tcrd-GDL mice per group, in 2-4 independent experiments for each time point. Significance was tested by the analysis of variance (ANOVA), the Brown-Forsythe and Welch ANOVA test, or the Kruskal-Wallis test with multiple comparisons test depending on the results of normality and homogeneity of variance tests. $^{*}P<0.05$.
Abbreviations: PBS, phosphate buffered saline; NK, natural killer; MHC, major histocompatibility complex; DC, dendritic cell; ns, non-significant.

Comparisons of absolute numbers of various immune cells in the dura among the control group, the day 1 group, and the day 3 PBS group are shown in **Figure 17**. The number of monocytes is significantly increased in the day 1 group. No other significant difference is found among the three groups. However, the number of γδ T cells seems to increase in the day 1 group. And a decreasing trend from day 1 to day 3 post-tMCAO modeling also might exist. These trends correlate with the findings in the integrated scRNAseq dataset. To sum up, the aforementioned analyses in this part indicate that AIS might influence the immune cell compositions of dura. The number and percentage of γδ T cells might increase on day 1 post-tMCAO but then might relatively decrease on day 3 post-tMCAO.

4.4 Following AIS, the migratory potential of dural γδ T cells may be enhanced from the baseline to day 3 post-tMCAO

4.4.1 Cell adhesion pathway is significantly suppressed in γδ T cells on day 1 post-tMCAO

To investigate the alterations of dural γδ T cells at different time points post-tMCAO, GSEA analyses were conducted on γδ T cells in the following comparisons: the tMCAO day 1 group vs. the control group, the tMCAO day 3 group vs. the control group, and the tMCAO day 3 group vs. the tMCAO day 1 group. In **Figure 18**, the top five significantly altered pathways of γδ T cells in the tMCAO day 1 group are displayed, in comparison to the control group. These results indicate that the cell adhesion-related pathways are significantly downregulated in dural γδ T cells on day 1 post-tMCAO modeling. The

regulation of lymphocyte activation pathway is also significantly suppressed.

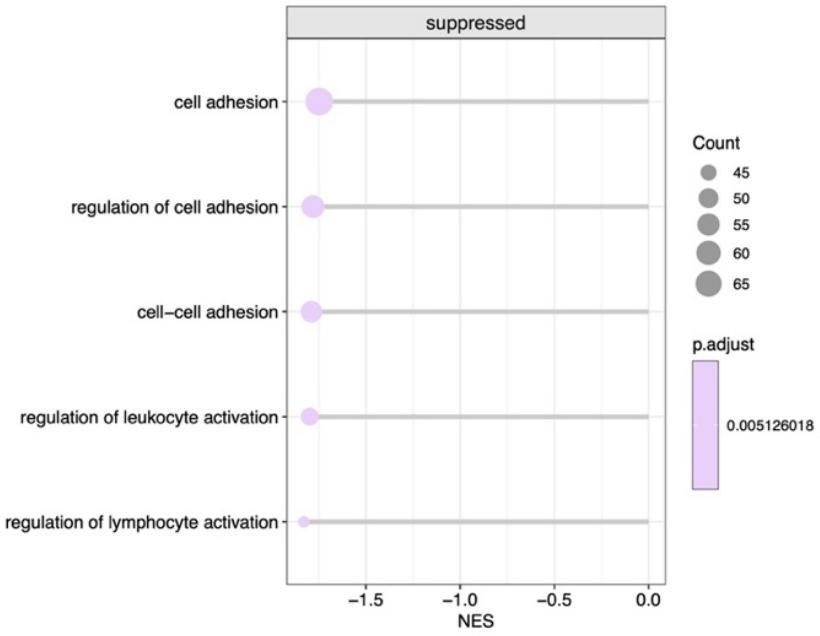

Figure 18. The top five significantly altered pathways in γδ T cells between the tMCAO day 1 group and the control group. In this comparison, 363 γδ T cells from the tMCAO day 1 group and 194 γδ T cells from the control group were used. The biological process database in the Gene Ontology database was used as a reference for GSEA, and the gseGO function in the ClusterProfile R package was utilized to perform GSEA analyses on γδ T cells between the tMCAO day 1 group and the control group. Detailed parameters of gseGO function were listed as (OrgDb= org.Mm.eg.db, ont = 'BP', minGSSize = 100, maxGSSize = 500). The size of dots represents the number of genes in a specific biological process pathway, and the color represents the adjusted *P* value. The net enrichment score (NES) quantifies the degree to which a particular pathway is overrepresented or underrepresented in the tMCAO day 1 group. A positive NES represents that a specific pathway is upregulated in the tMCAO day 1 group, while a negative NES suggests that a specific pathway is downregulated in the tMCAO day 1 group.
Abbreviations: NES, net enrichment score; GSEA, gene set enrichment analyses; tMCAO, temporary middle cerebral artery occlusion.

To assess changes in cell adhesion through flow cytometric experiments, this study examined the expression of CD69 in γδ T cells, which serves as a retention marker for tissue immune cells (Cibrian and Sanchez-Madrid 2017). Analyses on the T cell stimulation panel show that the percentages of $CD69^+$ γδ T cells are comparable among the control, day 1, and day 3 PBS groups. However, MFI values of CD69 in $CD69^+$ γδ T cells are significantly lower in the day 1 group compared with the control group (**Figure**

19), reflecting a decrease in median CD69 molecules per cell. The results from the scRNAseq and flow cytometric data suggest that dural γδ T cells might have decreased adhesion to other cells/stroma and relatively reduced activation status on day 1 post-tMCAO when compared to the control group.

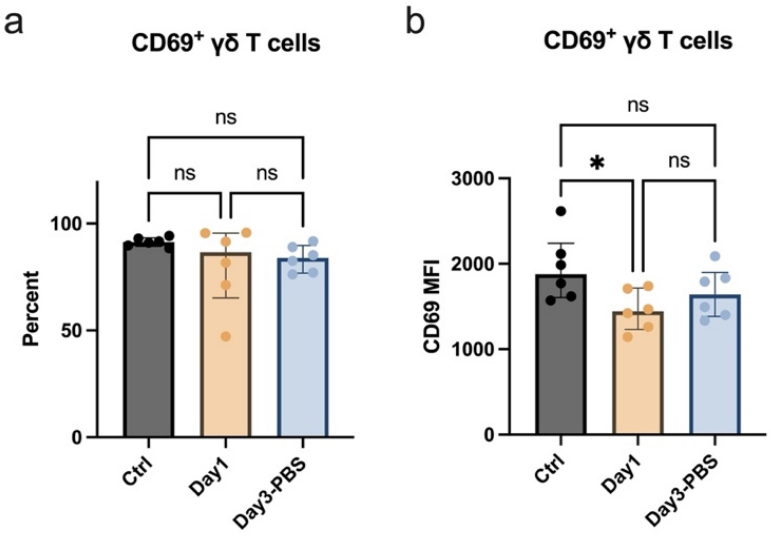

Figure 19. Comparisons on the percentages (a) and CD69 MFI values (b) of $CD69^+$ γδ T cells in the dura among the control group, the day 1 group, and the day 3 PBS group. Data were obtained after flow cytometric analysis of dural immune cells stained for IFN-γ, CD4, GM-CSF, IL-17A, CD11b, CD69, NK1.1, TCRγδ, B220, CD3, CD45, and CD8a. Detailed gating strategies are shown in **Figure 7**. The median function in the Flowjo was used to calculate MFI values of CD69 for $CD69^+$ γδ T cells. The figures show median ± interquartile range of six Tcrd-GDL mice per group, in 2-4 independent experiments for each time point. Significance was tested by the analysis of variance (ANOVA), the Brown-Forsythe and Welch ANOVA test, or the Kruskal-Wallis test with multiple comparisons test depending on the results of normality and homogeneity of variance tests. $^*P<0.05$.
Abbreviations: PBS, phosphate buffered saline; MFI, Median Fluorescence Intensity; ns, non-significant.

4.4.2 Cell migration pathway is significantly up-regulated in γδ T cells at day 3 post-tMCAO

Considering the decreasing trends of counts and percentages of γδ T cells on day 3 post-tMCAO compared to day 1 post-tMCAO, this study checked the cell migration pathway activation status in γδ T cells from the tMCAO day 3 group with the GSEA method. The results demonstrate that the cell migration pathway is significantly upregulated in the

tMCAO day 3 group compared to both the control group (**Figure 20a**) and the tMCAO day 1 group (**Figure 20b**). These results indicate that the migration ability of dural γδ T cells might be significantly enhanced on day 3 post-tMCAO modeling.

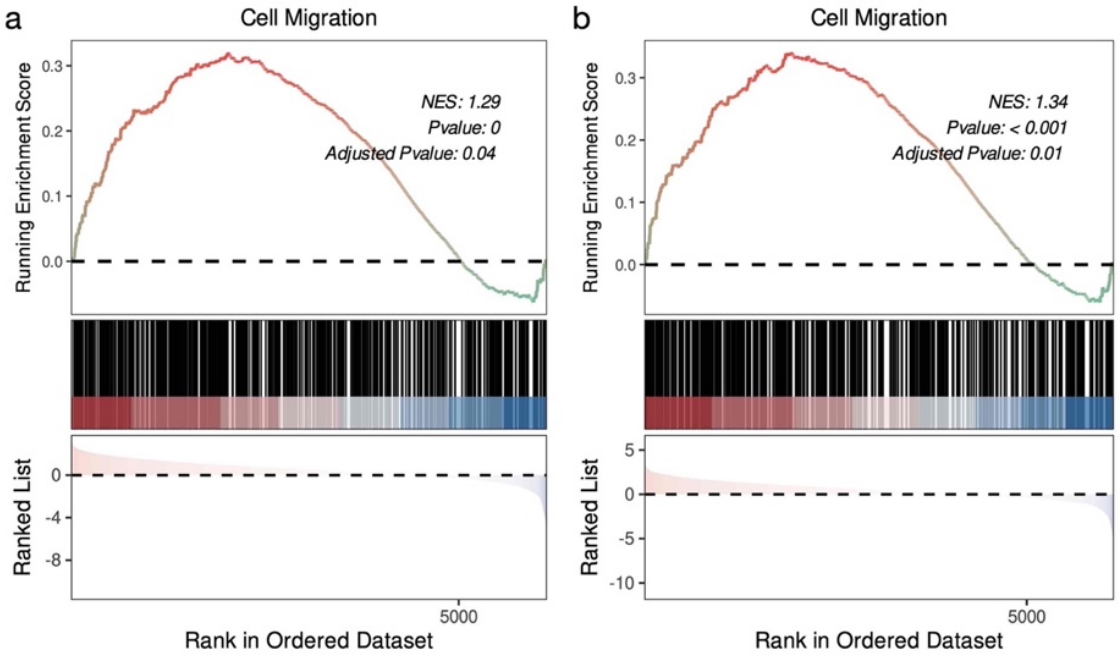

Figure 20. The cell migration pathway is significantly enhanced in the tMCAO day 3 group. (a) Comparison of the activation status of the cell migration pathway between the tMCAO day 3 group and the control group with the GSEA method. (b) Comparison of the activation status of the cell migration pathway between the tMCAO day 3 group and the tMCAO day 1 group with the GSEA method. All 599 γδ T cells in the integrated post-tMCAO dural scRNAseq data were used (194 in the control group, 363 in the tMCAO day 1 group, and 42 in the tMCAO day 3 group). The biological process database in the Gene Ontology database was used as a reference for GSEA, and the gseGO function in the ClusterProfile R package was utilized to perform GSEA analyses on γδ T cells between the tMCAO day 3 group and the control/tMCAO day 1 group, respectively. Detailed parameters of gseGO function were listed as (OrgDb= org.Mm.eg.db, ont = 'BP', minGSSize = 100, maxGSSize = 500). The net enrichment score (NES) quantifies the degree to which a particular pathway is overrepresented or underrepresented in the tMCAO day 3 group. A positive NES represents that a specific pathway is upregulated in the tMCAO day 3 group, while a negative NES suggests that a specific pathway is downregulated in the tMCAO day 3 group.
Abbreviations: tMCAO, temporary middle cerebral artery occlusion; GSEA, gene set enrichment analyses; NES, net enrichment score.

4.5 The majority of dural γδ T cells can produce IL-17A upon stimulation, and these cells demonstrate consistent IL-17A-producing capabilities at baseline, day 1, and

day 3 post-tMCAO modeling

To better characterize the functions of γδ T cells in the dura, productions of IL-17A, GM-CSF, and IFN-γ in γδ T cells were also analyzed with the T cell stimulation panel of flow cytometry. Upon stimulation, approximately 60-80% of γδ T cells can produce IL-17A. The percentages of IL-17A$^+$ γδ T cells and MFI values of IL-17A in IL-17A$^+$ γδ T cells are comparable among the control group, the day 1 group, and the day 3 PBS group (**Figure 21**). Higher percentages of GM-CSF$^+$ γδ T cells are detected in the day 3 PBS group compared to the day 1 group. No other significant difference among the three groups is found. These findings suggest that a significant portion of dural γδ T cells can produce IL-17A in response to stimulation. Furthermore, the IL-17A-producing capabilities appear to be comparable among the control group, the day 1 group, and the day 3 PBS group.

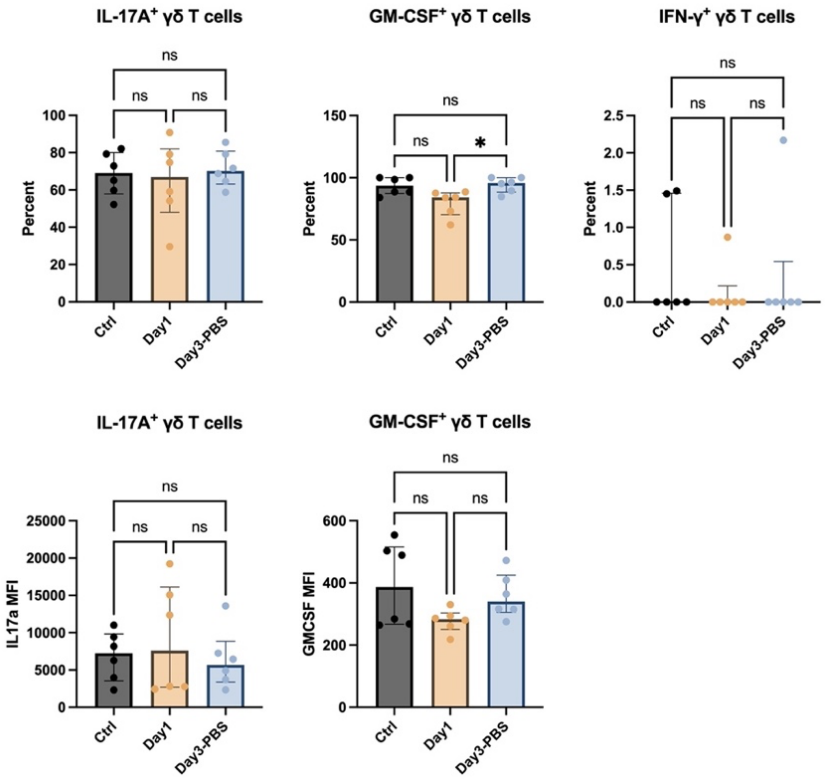

Figure 21. Comparisons on the percentages of IL-17A$^+$ γδ T cells, GM-CSF$^+$ γδ T cells, and IFN-γ$^+$ γδ T cells, as well as the MFI values of relevant cytokines in the dura among the control group, day 1 group, and day 3 PBS group. MFI values of IFN-γ in IFN-γ$^+$ γδ T cells were not calculated due to the very low expression percentage. Data were obtained after flow cytometric analysis of dural immune cells stained for IFN-γ, CD4, GM-CSF, IL-17A, CD11b, CD69, NK1.1, TCRγδ,

B220, CD3, CD45, and CD8a. Detailed gating strategies are shown in **Figure 7**. The median function in the Flowjo was used to calculate the MFI values of IL-17A for IL-17A$^+$ γδ T cells, and the MFI values of GM-CSF for GM-CSF$^+$ γδ T cells. The figures show median ± interquartile range of six Tcrd-GDL mice per group, in 2-4 independent experiments for each time point. Significance was tested by the analysis of variance (ANOVA), the Brown-Forsythe and Welch ANOVA test, or the Kruskal-Wallis test with multiple comparisons test depending on the results of normality and homogeneity of variance tests. $^*P<0.05$.
Abbreviations: PBS, phosphate buffered saline; MFI, Median Fluorescence Intensity; GM-CSF, granulocyte-macrophage colony-stimulating factor; ns, non-significant.

4.6 The activation status of γδ T cells significantly decreases on day 1 post-tMCAO but increases on day 3 post-tMCAO

Phenotypes of γδ T cells are various. Previous studies have emphasized that IL-17$^+$ γδ T cells are important inflammation amplifiers after AIS (Gelderblom et al. 2012, Shichita et al. 2009). Considering that the majority of dural γδ T cells exhibit comparable IL-17A-producing potential at baseline, day 1, and day 3 post-stroke after stimulation, this study employed the integrated scRNAseq data to assess the expression of marker genes specific to IL-17$^+$ γδ T cells in dural γδ T cells at various time points post-stroke. The expression of marker genes (includes *Cd44, Il23r, Ccr2, Rora, Il7r, Il2ra, Sox13, Ccr6, Rorc, Il17a, S100a6, Il18r1, Icos, Blk, Maf,* and *Cxcr6*) were quantified with the 'AddModuleScore' function in the Seurat for all γδ T cells in the control group, the tMCAO day 1 group, and the tMCAO day 3 group, which formed the γδ17 signature scores. A higher score for a sample suggests that these genes are relatively upregulated in that sample, which could be used to represent a higher activation status of γδ T cells. Comparisons on the γδ17 signature scores among the control group, the tMCAO day 1 group, and the tMCAO day 3 group were performed, and the results are shown in **Figure 22**. The γδ17 signature scores are significantly lower in the tMCAO day 1 group compared to the control group and the tMCAO day 3 group, and the scores in the tMCAO day 3 group are significantly higher than the control group and the tMCAO day 1 group. The results of γδ17 signature scores might suggest that the average activation status of dural γδ T cells significantly decreases on day 1 post-tMCAO but increases significantly on day 3 post-tMCAO.

Considering the increased number of γδ T cells on day 1 post-tMCAO, the migration of less-activated γδ T cells from the periphery into the dura may partly explain the relatively diminished γδ17 signature scores on that day.

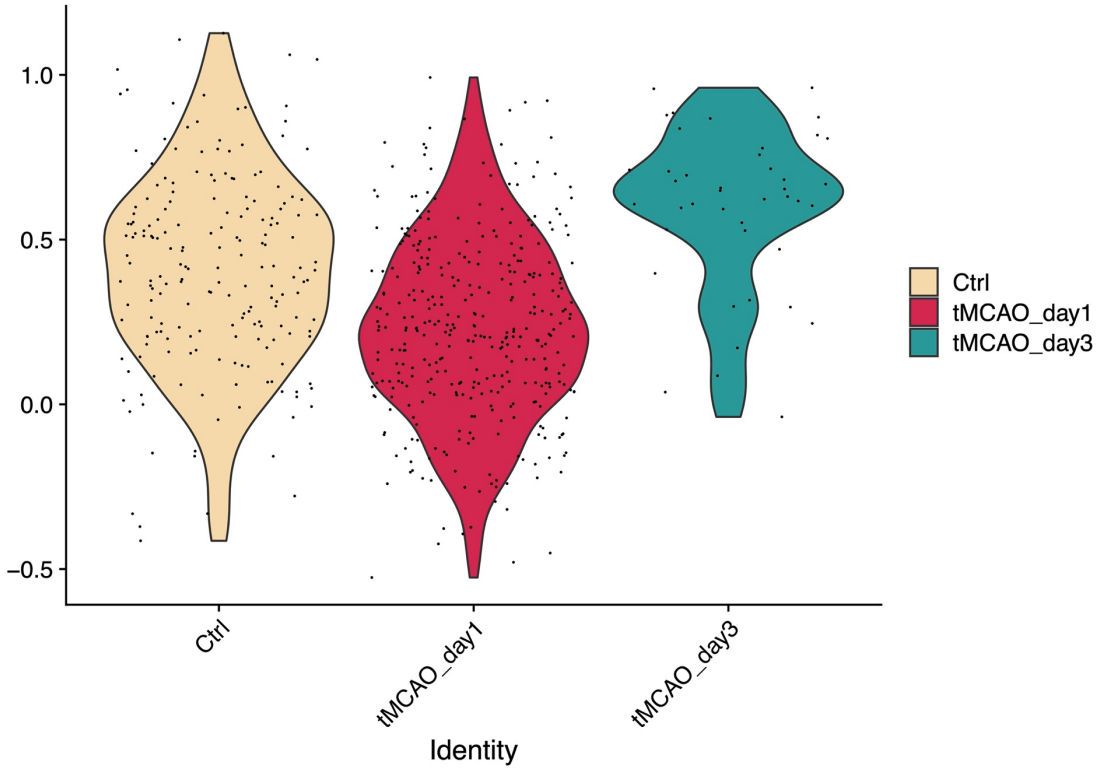

Figure 22. Comparisons of the γδ17 signature scores among all γδ T cells in the control group, the tMCAO day 1 group, and the tMCAO day 3 group. All 599 γδ T cells in the integrated dural scRNAseq data were used (194 in the control group, 363 in the tMCAO day 1 group, and 42 in the tMCAO day 3 group). Each dot on the figure represents one γδ T cell. The γδ17 signature includes *Cd44, Il23r, Ccr2, Rora, Il7r, Il2ra, Sox13, Ccr6, Rorc, Il17a, S100a6, Il18r1, Icos, Blk, Maf,* and *Cxcr6* genes. These gene signatures are known markers of IL-17^{+} γδ T cells. The 'AddModuleScore' function calculates the average expression of a given signature per cell and subtracts it from the average expression of randomly selected control features. A higher score of a sample suggests that these genes are relatively upregulated in that sample. After calculation, the Dunn Kruskal-Wallis multiple comparison test from the FSA R package was used to test the significance of difference.
Abbreviation: tMCAO, temporary middle cerebral artery occlusion.

4.7 The impact of γδ T cells on the dural immune landscape is minor

The preceding results might indicate that γδ T cells undergo significant activation in the

dura on day 3 post-tMCAO. To explore the impact of γδ T cells on the dural immune landscape, DTX was injected into the Tcrd-GDL mice as planned to deplete the γδ T cells. No alterations in spontaneous behaviors and facial expressions were found in the day 3 DTX group. The weight of mice before tMCAO modeling was comparable between the day 3 DTX group and the day 3 DTX group. Representative pictures of the depletion effect are shown in **Figure 23a-b**, and the absolute counts of γδ T cells are significantly lower in the day 3 DTX group compared to the day 3 PBS group (**Figure 23c**).

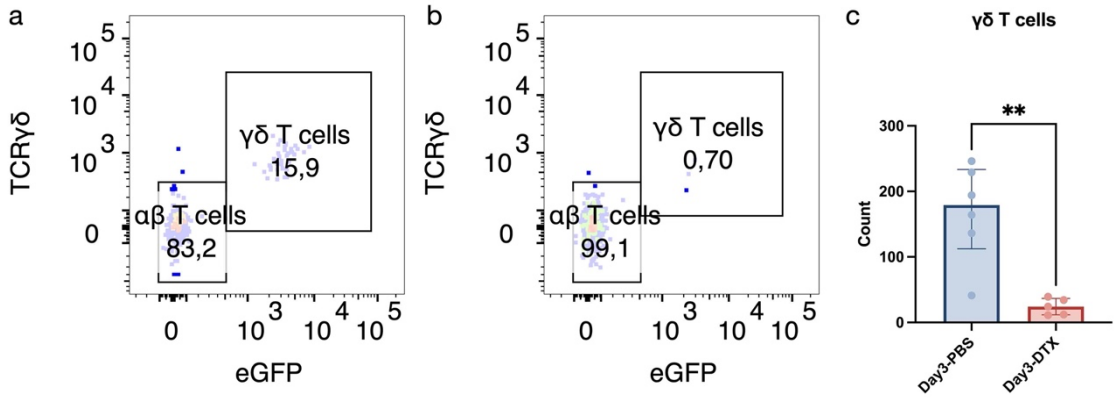

Figure 23. Representative pictures of successful γδ T cell depletion in the Tcrd-GDL mouse line and comparisons on the absolute number of γδ T cells in the dura between the day 3 PBS group and the day 3 DTX group. (a) Gating of γδ T cells in a mouse from the day 3 PBS group. (b) Gating of γδ T cells in a mouse from the day 3 DTX group. (c) Cell counting comparisons between the day 3 PBS group and the day 3 DTX group. Data were obtained after flow cytometric analysis of dural immune cells stained for Ly6G, CD4, CD11b, CD3ε, CD45, Ly6C, MHC II, CD8a, TCRγδ, B220, NK1.1, F4/80, and CD11c. Detailed gating strategies are shown in **Figure 6**. For cell counting, BD Trucount™ Absolute Counting Tubes were used. Cell counts were calculated with the beads recorded in the BD FACS Symphony A3 and the original beads number included in the BD Trucount™ tube. The figures show median ± interquartile range of six Tcrd-GDL mice in the day 3 PBS group and five in the day 3 DTX group, in 4 independent experiments for each time point. Significance was tested by the unpaired t-test, the unpaired t-test with Welch's correction, or the Mann-Whitney test depending on the results of normality and homogeneity of variance tests. $^{**}P<0.01$.
Abbreviations: eGFP, enhanced green fluorescent protein; PBS, phosphate buffered saline; DTX, diphtheria toxin.

As for other types of immune cells, the number of $CD4^+$ T cells is significantly higher in the day 3 DTX group, and no other significant difference is found between the day 3 DTX and the day 3 PBS groups (**Figure 24**). These results indicate that the impact of γδ T cells

on the dural immune landscape is relatively mild.

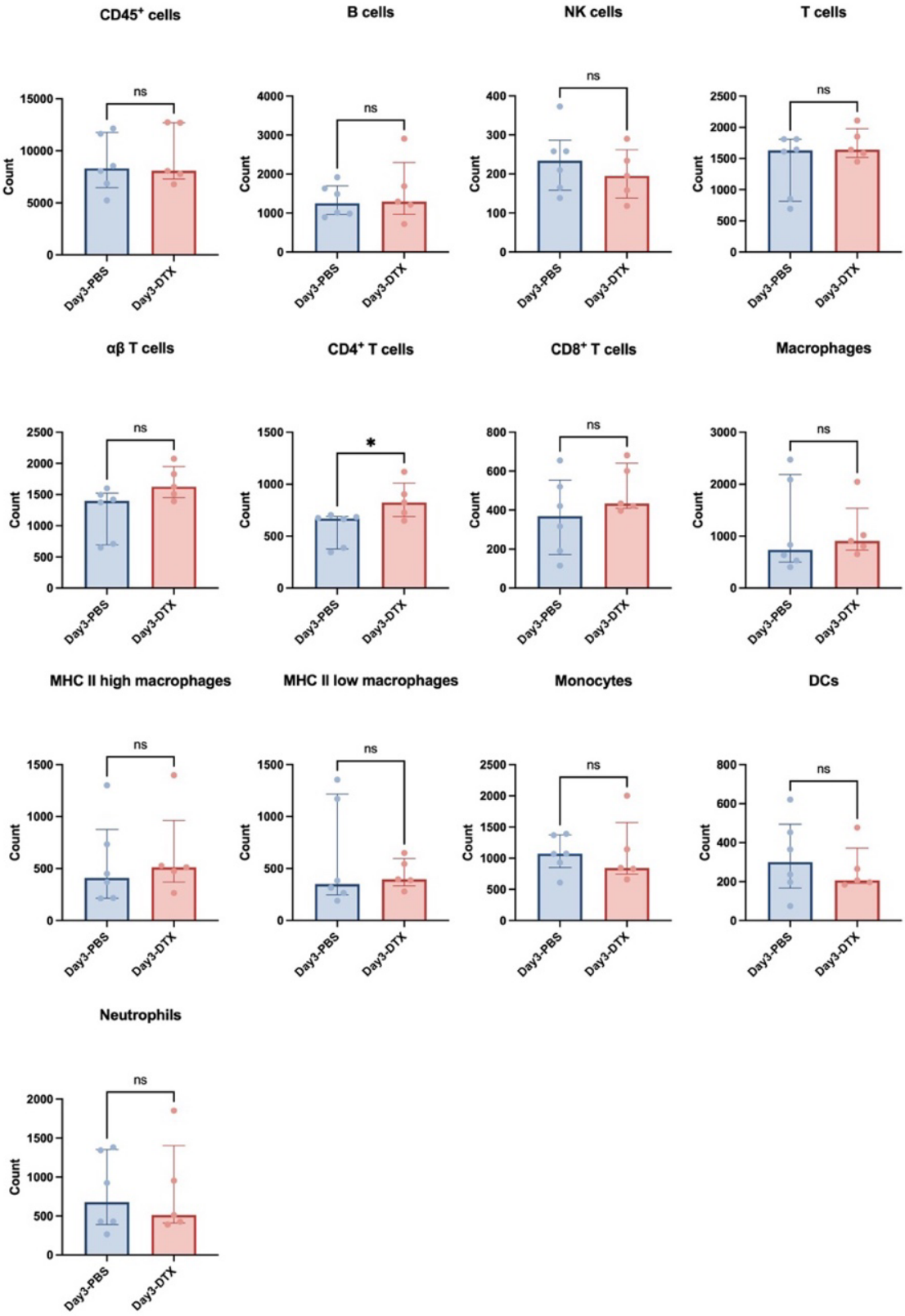

Figure 24. Comparisons on absolute numbers of different kinds of immune cells in dura between

the day 3 PBS group and the day 3 DTX group. Data were obtained after flow cytometric analysis of dural cells stained for Ly6G, CD4, CD11b, CD3ε, CD45, Ly6C, MHC, CD8a, TCRγδ, B220, NK1.1, F4/80, and CD11c. For cell counting, BD Trucount™ Absolute Counting Tubes were used. Cell counts were calculated with the beads recorded in the BD FACS Symphony A3 and the original beads number included in the BD Trucount™ tube. Detailed gating strategies are shown in **Figure 6**. The figures show median ± interquartile range of six Tcrd-GDL mice in the day 3 PBS group and five in the day 3 DTX group, in 4 independent experiments for each time point. Significance was tested by the unpaired t-test, the unpaired t-test with Welch's correction, or the Mann-Whitney test depending on the results of normality and homogeneity of variance tests. $^{*}P<0.05$.

Abbreviations: PBS, phosphate buffered saline; DTX, diphtheria toxin; NK, natural killer; MHC, major histocompatibility complex; DC, dendritic cell; ns, non-significant.

5. Discussion

In this study, analyses of the integrated dural scRNAseq atlas reveal that the dural immune landscapes are heterogeneous among different conditions. By integrating dural scRNAseq data from two tMCAO modeling studies and performing flow cytometric experiments at different time points post-tMCAO, this study also reveals that the immune compositions of dura might change after AIS onset. The fluctuations in the number and changes in migration and activation abilities of dural γδ T cells during the progression of AIS suggest that dural γδ T cells might play important roles in AIS. The impact of γδ T cells on the dural immune compartment after AIS onset seems to be relatively mild. After depleting γδ T cells, only the quantity of $CD4^+$ T cells shows a significant alteration.

Immune landscapes of the dura exhibit heterogeneity across various conditions, and the reasons for this heterogeneous immune compartment might be disease specific. The aged dura is characterized by lower proportions of DC subtypes and macrophages, which are crucial antigen processing and presentation (APC) cells. Previous studies have shown that dural sinuses might play roles in immune surveillance, and meningeal lymphatic vessels participate in metabolic waste clearance from the CNS (Da Mesquita et al. 2018, Rustenhoven et al. 2021). The reduced proportions of APC cells in the aged dura may contribute to the accumulation of waste in the brain and cognitive decline associated with aging. An upward trend in the percentages of neutrophils and a downward trend in the percentages of NK cells are observed in the aged dura. Nevertheless, the underlying biological significance of these trends is yet to be fully understood.

The percentages of B cells seem to decrease at different stages of EAE. This relative reduction might be explained by the accumulation of myeloid cells (Jordao et al. 2019). Another possible explanation for this phenomenon is that B cells infiltrate into other layers of the meninges or the brain and contribute to autoimmunity after the initiation of EAE. The relationship between the dura and B cells might be intricate, as indicated by the presence of B cells in diverse developmental stages residing within the dura (Brioschi et al. 2021). In conclusion, additional research is needed to explore the heterogeneity of

the dural immune landscape and its influence on the underlying diseases.

Recent studies have indicated that neutrophils and other myeloid cells can migrate from the skull bone marrow to the dura following the tMCAO modeling (Herisson et al. 2018, Kolabas et al. 2023), suggesting potential changes in dural cell compositions after AIS. In this study, flow cytometric analyses of the dural immune landscape reveal that numbers of monocytes are increased in the dura at day 1 post-tMCAO modeling. However, the counts of monocytes are comparable between day 3 post-tMCAO and the control group. The migrations, functions and differentiations of dural monocytes after AIS onset are interesting questions that remain to be answered, and further live imaging studies might offer additional insights into this phenomenon.

Given the significant roles of IL-17A$^+$ γδ T cells in the context of AIS (Gelderblom et al. 2012) and the presence of IL-17$^+$ γδ T cells in meninges under homeostasis (Alves de Lima et al. 2020, Ribot et al. 2021), this study investigates the properties of dural γδ T cells through scRNAseq analyses and flow cytometric experiments. The scRNAseq analyses show that number of dural γδ T cells might increase on day 1 post-tMCAO, and then decrease relatively on day 3 post-tMCAO. The dynamically changing pattern in cell counts and percentages suggests that γδ T cells undergo alterations in the early stages of AIS. A previous study has shown that IL-17$^+$ γδ T cells might migrate from intestine to the meninges and modulate ischemic injury after AIS (Benakis et al. 2016). These infiltrated γδ T cells may account for the increased numbers in the dura at day 1 post-tMCAO. As for day 3 post-tMCAO, the enhanced migratory capacity of γδ T cells during that period could partially explain the reduced number of γδ T cells.

Analyses of the integrated post-tMCAO dural scRNAseq data indicate that the cell adhesion ability of dural γδ T cells may be significantly diminished on day 1 post-tMCAO modeling compared to the control group. This observation is consistent with the lower CD69 MFI values found in the day 1 group in flow cytometric analyses. CD69 is known as a molecule related to the retention/survival of tissue-resident immune cells (Cibrian and Sanchez-Madrid 2017). Reduced expression of retention-related markers might

facilitate the migration of γδ T cells. Enrichment analyses also indicate that the cell migration pathway is significantly enhanced in dural γδ T cells at day 3 post-tMCAO modeling. A recent study has illustrated migration behaviors of γδ T cells across the meningeal structure toward the brain after cerebral microbleeds (Su et al. 2023). The percentage of γδ T cells in the ischemic brain significantly increases on day 3 post-tMCAO compared to day 1 post-tMCAO (Gelderblom et al. 2012). One plausible hypothesis for the aforementioned results and trends is that following tMCAO modeling, the migratory potential of γδ T cells may increase from the baseline to day 3 post-tMCAO, enabling these cells to infiltrate the ischemic brain.

Other than the changes in adhesion and migration abilities, dural γδ T cells might also undergo activations and acquire the IL-17A$^+$ phenotype after AIS. According to the results of flow cytometric experiments, the majority of γδ T cells (around 60-80%) can produce IL-17A after stimulation, and the IL-17A-producing potentials are similar among the baseline, day 1, and day 3 post-tMCAO modeling. However, the GSEA reveals that the regulation of lymphocyte activation pathway is downregulated on day 1 post-tMCAO. Analyses on the γδ17 signature scores also indicate that the activation status of IL-17A$^+$ γδ T cells significantly decreases on day 1 post-tMCAO but increases on day 3 post-tMCAO. The downregulated pathway and relatively lower enrichment of IL-17$^+$ phenotype genes on day 1 post-tMCAO might be explained by the 'dilution effect'. After AIS onset, γδ T cells without IL-17$^+$ phenotype migrate from the periphery towards dura, reducing the average expressions of marker genes of IL-17$^+$ γδ T cells. These γδ T cells gradually acquire activation phenotypes and enhance their migration abilities in the dura, and then migrate towards the brain or other layers of meninges. Descriptions of this hypothesis are shown in **Figure 25**. However, the correctness of this hypothesis still needs further investigation.

Besides, the percentages of GM-CSF$^+$ γδ T cells are also significantly higher on day 3 post-tMCAO compared to the day 1 group. A previous study has shown that IL-23R$^+$ γδ T cells in the aortic root might produce IL-17A and GM-CSF and promote early

atherosclerotic lesion formation and plaque necrosis (Gil-Pulido et al. 2022). In current study, the expression of GM-CSF might also serve as a marker for the activation of γδ T cells after tMCAO modeling, and the impact of GM-CSF produced by dural γδ T cells following AIS is yet to be explored.

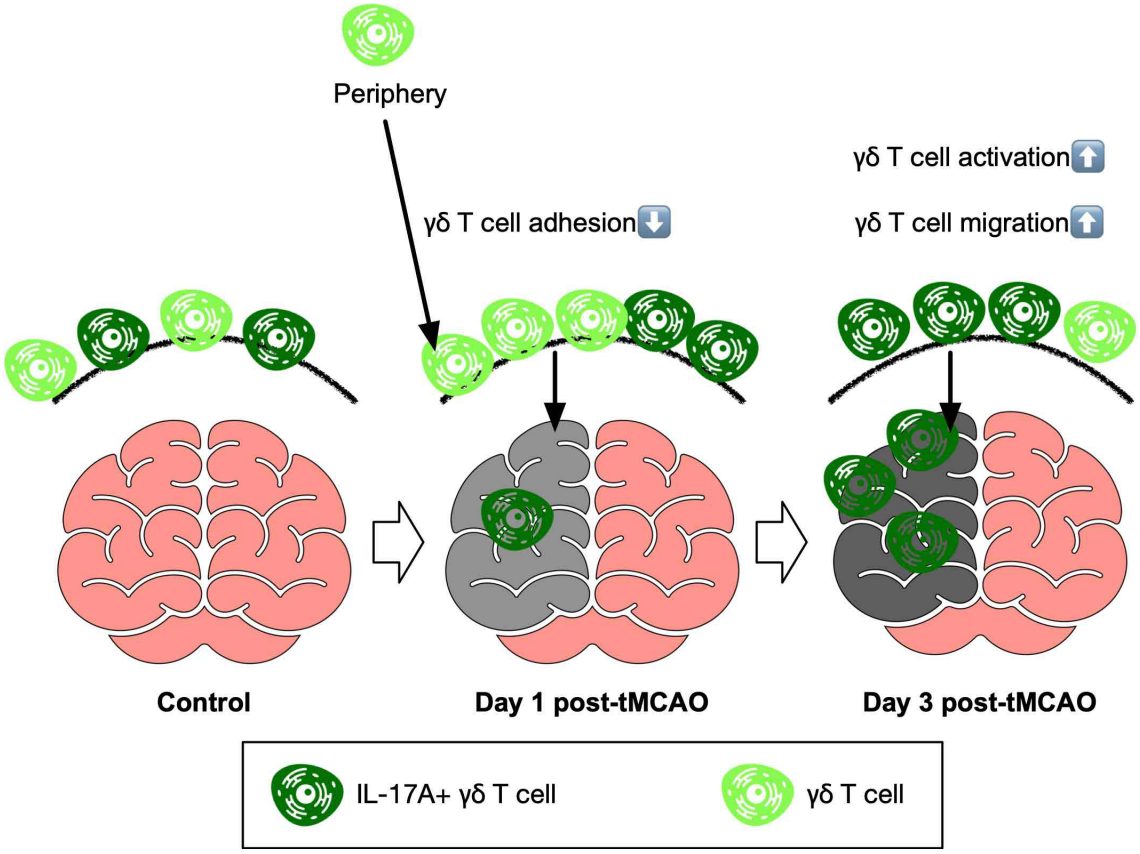

Figure 25. The illustration of hypothesis of this study. As shown in the figure, in baseline conditions, γδ T cells and IL-17A$^+$ γδ T cells reside in the dura. At day 1 post-tMCAO, γδ T cells without IL-17A$^+$ phenotype might migrate from the periphery to the dura, increasing the number and reducing the average expressions of marker genes of IL-17$^+$ γδ T cells. The decreasing cell adhesion activities in γδ T cells facilitate the migration process. On day 3 post-tMCAO, more γδ T cells acquire IL-17A$^+$ phenotype and have enhanced cell migration abilities. These activated γδ T cells might migrate towards the infarction zone and participate in the inflammatory process. Abbreviation: tMCAO, temporary middle cerebral artery occlusion.

Dural γδ T cells might be significantly activated on day 3 post-AIS, and this study also explores the impact of γδ T cells on the dural immune compartment on day 3 post-AIS. After the successful depletion of γδ T cells, the numbers of CD4$^+$ T cells are significantly

increased in the dura. Whereas, the roles of these increased $CD4^+$ T cells are still uncertain. DTX has been shown to not affect $CD4^+$ or $CD8^+$ T cells in the Tcrd-GDL mouse line (Sandrock et al. 2018). Furthermore, the number of other immune cells remains comparable between the depletion and non-depletion mice. In general, the impact of γδ T cells on the dural immune landscape is mild.

Through the integration of data from various resources and the implementation of well-structured analytical methods, this study provides a comprehensive characterization of the immune landscape within the dura under varying conditions, especially at different time points post-AIS. Integrating analyses of flow cytometric data from multiple groups and scRNAseq data enhances the robustness of the findings. However, there are also limitations in this study. First of all, flow cytometric experiments were conducted only on the control group and the tMCAO group. Further investigations involving other disease models are required. Furthermore, despite the implementation of rigorous quality control thresholds and multi-step adjustments, potential batch effects and heterogeneities in the integrated scRNAseq data may still exist. Additionally, several groups within the dural scRNAseq atlas lack biological replicates, which restricts the choice of analytical methods and hinders the generalizability of the results. Given that the dura serves as an immune interface, it is necessary to consider the bone marrow and other adjacent tissues when analyzing its roles. The absence of bone marrow flow cytometric data might impact the interpretation of the findings. After stroke initiation, the relationship between dural γδ T cells and CNS-infiltrating γδ T cells is still awaiting confirmation. Understanding the potential migration pathway of γδ T cells between the dura and the brain holds significant importance. Exploring the factors responsible for triggering detrimental phenotype changes in dural γδ T cells following AIS could provide valuable insights into stroke interventions. These questions warrant further explorations.

To summarize, this study reveals changes in the composition of the dural immune compartment under different conditions, hypothesizes potential migration and activation patterns of dural γδ T cells after the onset of AIS, and investigates the impact of dural γδ

T cells on the dural immune landscape. As a crucial immune interface next to the CNS, the diverse roles of the dura remain intricate and call for further investigations.

6. Summary

The dura functions as a crucial immune niche located adjacent to the brain. However, the impact of pathological changes in the brain parenchyma on the dural immune compartment remains uncertain. This study aims to investigate the alterations in the compositions of dural immune cells under various pathological conditions and during the aging process. Besides, this study seeks to explore the roles of dural γδ T cells in the context of acute ischemic stroke (AIS).

This study systematically searched and integrated dural single-cell RNA sequencing datasets from 10 published studies up to May 15, 2023, and established a single-cell atlas containing 120,893 cells. The single-cell atlas revealed notable heterogeneities in the percentages of various immune cells across six conditions, including baseline, aged, experimental autoimmune encephalomyelitis, traumatic brain injury, photothrombotic injury, and temporary middle cerebral artery occlusion. Furthermore, this study incorporated and analyzed dural single-cell RNA sequencing data at baseline, 1 day, and 3 days following AIS onset. The analysis showed an initial increasing followed by a subsequent decreasing trend in the proportion of dural γδ T cells post-AIS onset, which was confirmed by flow cytometric data. Enrichment analyses unveiled that the migratory capabilities and activation status of dural γδ T cells significantly increased as AIS progression. Additionally, this study conducted γδ T cell depletion prior to AIS modeling. The analysis of the frequency of dural immune cells in depleted mice showed that the impact of γδ T cells on the frequency of dural immune cells at day 3 post-AIS was minor, as the number of various dural immune cells were comparable, except for $CD4^+$ T cells.

Taken together, this study provides valuable insights into the disease-specific dural immune landscape. This study also postulates potential migration and activation patterns of dural γδ T cells following the onset of AIS. The observed increased migration abilities and heightened activation status of dural γδ T cells during the progression of AIS imply that these cells could serve as promising targets for interventions in the treatments of AIS.

Zusammenfassung

Die Dura fungiert als wichtige immunologische Barriere, die an das Gehirn angrenzt. Die Auswirkungen pathologischer Veränderungen des Hirnparenchyms auf das durale Immunkompartiment sind jedoch noch unklar. Ziel dieser Studie ist es, die Veränderungen in der Zusammensetzung der duralen Immunzellen unter verschiedenen pathologischen Bedingungen und während des Alterungsprozesses zu untersuchen. Außerdem soll die Rolle der duralen γδ-T-Zellen im Zusammenhang mit dem akuten ischämischen Schlaganfall (AIS) untersucht werden.

In dieser Studie wurden systematisch durale Einzelzell-RNA-Sequenzierungsdatensätze aus 10 veröffentlichten Studien bis zum 15. Mai 2023 durchsucht und integriert und ein Einzelzellatlas mit 120.893 Zellen erstellt. Der Einzelzell-Atlas zeigte bemerkenswerte Heterogenitäten in den Prozentsätzen verschiedener Immunzellen unter sechs Bedingungen, einschließlich Ruhebedingungen, Alter, experimentelle Autoimmun-Enzephalomyelitis, traumatische Hirnverletzung, photothrombotische zerebraler Ischämie und zerebraler Ischämie bei vorübergehender Verschluss der mittleren Hirnarterie. Darüber hinaus wurden in dieser Studie durale Einzelzell-RNA-Sequenzierungsdaten zu Studienbeginn, 1 Tag und 3 Tage nach Ausbruch des AIS einbezogen und analysiert. Die Analyse ergab einen anfänglichen Anstieg, gefolgt von einem anschließenden Abwärtstrend im Anteil der duralen γδ-T-Zellen in der Folge eines experimentellen Schlaganfalls, was in durchflusszytometrischen Daten bestätigt wurde. Weitere bioinformatische Analysen ergaben, dass die Migrationsfähigkeit und der Aktivierungsstatus der duralen γδ-T-Zellen mit dem Fortschreiten des AIS signifikant zunahmen. Darüber hinaus wurde in dieser Studie eine Depletion von γδ-T-Zellen vor der Modellierung des AIS durchgeführt. Die Analysen in den depletierten Mäusen zeigte, dass die Auswirkungen der γδ-T-Zellen auf die Zusammensetzung des duralen Immunkompartiments am Tag 3 nach dem AIS gering waren, da die Anzahl der verschiedenen duralen Immunzellen mit Ausnahme der CD4+-T-Zellen vergleichbar war. Insgesamt bietet diese Studie wertvolle Einblicke in die krankheitsspezifische durale Immunlandschaft. Diese Studie postuliert auch mögliche Migrations- und Aktivierungsmuster duraler γδ-T-Zellen nach dem Auftreten von AIS. Die beobachteten erhöhten Migrationsfähigkeiten und der erhöhte Aktivierungsstatus der duralen γδ-T-Zellen während des Fortschreitens von AIS deuten darauf hin, dass diese Zellen als vielversprechende Ziele für Interventionen bei der Behandlung von AIS dienen könnten.

7. Bibliography

Akopov SE, Simonian NA, Grigorian GS (1996) Dynamics of polymorphonuclear leukocyte accumulation in acute cerebral infarction and their correlation with brain tissue damage. Stroke. 27(10):1739-1743.

Alves de Lima K, Rustenhoven J, Da Mesquita S, Wall M, Salvador AF, Smirnov I, Martelossi Cebinelli G, Mamuladze T, Baker W, Papadopoulos Z, Lopes MB, Cao WS, Xie XS, Herz J, Kipnis J (2020) Meningeal gammadelta T cells regulate anxiety-like behavior via IL-17a signaling in neurons. Nat Immunol. 21(11):1421-1429.

Aran D, Looney AP, Liu L, Wu E, Fong V, Hsu A, Chak S, Naikawadi RP, Wolters PJ, Abate AR, Butte AJ, Bhattacharya M (2019) Reference-based analysis of lung single-cell sequencing reveals a transitional profibrotic macrophage. Nat Immunol. 20(2):163-172.

Ashburner M, Ball CA, Blake JA, Botstein D, Butler H, Cherry JM, Davis AP, Dolinski K, Dwight SS, Eppig JT, Harris MA, Hill DP, Issel-Tarver L, Kasarskis A, Lewis S, Matese JC, Richardson JE, Ringwald M, Rubin GM, Sherlock G (2000) Gene ontology: tool for the unification of biology. The Gene Ontology Consortium. Nat Genet. 25(1):25-29.

Baldominos P, Barbera-Mourelle A, Barreiro O, Huang Y, Wight A, Cho JW, Zhao X, Estivill G, Adam I, Sanchez X, McCarthy S, Schaller J, Khan Z, Ruzo A, Pastorello R, Richardson ET, Dillon D, Montero-Llopis P, Barroso-Sousa R, Forman J, Shukla SA, Tolaney SM, Mittendorf EA, von Andrian UH, Wucherpfennig KW, Hemberg M, Agudo J (2022) Quiescent cancer cells resist T cell attack by forming an immunosuppressive niche. Cell. 185(10):1694-1708 e1619.

Benakis C, Brea D, Caballero S, Faraco G, Moore J, Murphy M, Sita G, Racchumi G, Ling L, Pamer EG, Iadecola C, Anrather J (2016) Commensal microbiota affects ischemic stroke outcome by regulating intestinal gammadelta T cells. Nat Med.

22(5):516-523.

Berkhemer OA, Fransen PS, Beumer D, van den Berg LA, Lingsma HF, Yoo AJ, Schonewille WJ, Vos JA, Nederkoorn PJ, Wermer MJ, van Walderveen MA, Staals J, Hofmeijer J, van Oostayen JA, Lycklama a Nijeholt GJ, Boiten J, Brouwer PA, Emmer BJ, de Bruijn SF, van Dijk LC, Kappelle LJ, Lo RH, van Dijk EJ, de Vries J, de Kort PL, van Rooij WJ, van den Berg JS, van Hasselt BA, Aerden LA, Dallinga RJ, Visser MC, Bot JC, Vroomen PC, Eshghi O, Schreuder TH, Heijboer RJ, Keizer K, Tielbeek AV, den Hertog HM, Gerrits DG, van den Berg-Vos RM, Karas GB, Steyerberg EW, Flach HZ, Marquering HA, Sprengers ME, Jenniskens SF, Beenen LF, van den Berg R, Koudstaal PJ, van Zwam WH, Roos YB, van der Lugt A, van Oostenbrugge RJ, Majoie CB, Dippel DW, Investigators MC (2015) A randomized trial of intraarterial treatment for acute ischemic stroke. N Engl J Med. 372(1):11-20.

Beuker C, Schafflick D, Strecker JK, Heming M, Li X, Wolbert J, Schmidt-Pogoda A, Thomas C, Kuhlmann T, Aranda-Pardos I, N AG, Kumar PA, Werner Y, Kilic E, Hermann DM, Wiendl H, Stumm R, Meyer Zu Horste G, Minnerup J (2022) Stroke induces disease-specific myeloid cells in the brain parenchyma and pia. Nat Commun. 13(1):945.

Bieber M, Gronewold J, Scharf AC, Schuhmann MK, Langhauser F, Hopp S, Mencl S, Geuss E, Leinweber J, Guthmann J, Doeppner TR, Kleinschnitz C, Stoll G, Kraft P, Hermann DM (2019) Validity and Reliability of Neurological Scores in Mice Exposed to Middle Cerebral Artery Occlusion. Stroke. 50(10):2875-2882.

Bolte AC, Shapiro DA, Dutta AB, Ma WF, Bruch KR, Kovacs MA, Royo Marco A, Ennerfelt HE, Lukens JR (2023) The meningeal transcriptional response to traumatic brain injury and aging. Elife. 12.

Brioschi S, Wang WL, Peng V, Wang M, Shchukina I, Greenberg ZJ, Bando JK, Jaeger N, Czepielewski RS, Swain A, Mogilenko DA, Beatty WL, Bayguinov P, Fitzpatrick JAJ, Schuettpelz LG, Fronick CC, Smirnov I, Kipnis J, Shapiro VS,

Wu GF, Gilfillan S, Cella M, Artyomov MN, Kleinstein SH, Colonna M (2021) Heterogeneity of meningeal B cells reveals a lymphopoietic niche at the CNS borders. Science. 373(6553).

Brombacher TM, Nono JK, De Gouveia KS, Makena N, Darby M, Womersley J, Tamgue O, Brombacher F (2017) IL-13-Mediated Regulation of Learning and Memory. J Immunol. 198(7):2681-2688.

Cai R, Pan C, Ghasemigharagoz A, Todorov MI, Forstera B, Zhao S, Bhatia HS, Parra-Damas A, Mrowka L, Theodorou D, Rempfler M, Xavier ALR, Kress BT, Benakis C, Steinke H, Liebscher S, Bechmann I, Liesz A, Menze B, Kerschensteiner M, Nedergaard M, Erturk A (2019) Panoptic imaging of transparent mice reveals whole-body neuronal projections and skull-meninges connections. Nat Neurosci. 22(2):317-327.

Campbell BC, Mitchell PJ, Kleinig TJ, Dewey HM, Churilov L, Yassi N, Yan B, Dowling RJ, Parsons MW, Oxley TJ, Wu TY, Brooks M, Simpson MA, Miteff F, Levi CR, Krause M, Harrington TJ, Faulder KC, Steinfort BS, Priglinger M, Ang T, Scroop R, Barber PA, McGuinness B, Wijeratne T, Phan TG, Chong W, Chandra RV, Bladin CF, Badve M, Rice H, de Villiers L, Ma H, Desmond PM, Donnan GA, Davis SM, Investigators E-I (2015) Endovascular therapy for ischemic stroke with perfusion-imaging selection. N Engl J Med. 372(11):1009-1018.

Cibrian D and Sanchez-Madrid F (2017) CD69: from activation marker to metabolic gatekeeper. Eur J Immunol. 47(6):946-953.

Coles JA, Myburgh E, Brewer JM, McMenamin PG (2017) Where are we? The anatomy of the murine cortical meninges revisited for intravital imaging, immunology, and clearance of waste from the brain. Prog Neurobiol. 156:107-148.

Da Mesquita S, Louveau A, Vaccari A, Smirnov I, Cornelison RC, Kingsmore KM, Contarino C, Onengut-Gumuscu S, Farber E, Raper D, Viar KE, Powell RD, Baker W, Dabhi N, Bai R, Cao R, Hu S, Rich SS, Munson JM, Lopes MB, Overall CC, Acton ST, Kipnis J (2018) Functional aspects of meningeal lymphatics in

ageing and Alzheimer's disease. Nature. 560(7717):185-191.

Derecki NC, Cardani AN, Yang CH, Quinnies KM, Crihfield A, Lynch KR, Kipnis J (2010) Regulation of learning and memory by meningeal immunity: a key role for IL-4. J Exp Med. 207(5):1067-1080.

Filiano AJ, Xu Y, Tustison NJ, Marsh RL, Baker W, Smirnov I, Overall CC, Gadani SP, Turner SD, Weng Z, Peerzade SN, Chen H, Lee KS, Scott MM, Beenhakker MP, Litvak V, Kipnis J (2016) Unexpected role of interferon-gamma in regulating neuronal connectivity and social behaviour. Nature. 535(7612):425-429.

G. B. D. Stroke Collaborators (2019) Global, regional, and national burden of stroke, 1990-2016: a systematic analysis for the Global Burden of Disease Study 2016. Lancet Neurol. 18(5):439-458.

Gelderblom M, Koch S, Strecker JK, Jorgensen C, Garcia-Bonilla L, Ludewig P, Schadlich IS, Piepke M, Degenhardt K, Bernreuther C, Pinnschmidt H, Arumugam TV, Thomalla G, Faber C, Sedlacik J, Gerloff C, Minnerup J, Clausen BH, Anrather J, Magnus T (2023) A preclinical randomized controlled multi-centre trial of anti-interleukin-17A treatment for acute ischaemic stroke. Brain Commun. 5(2):fcad090.

Gelderblom M, Leypoldt F, Steinbach K, Behrens D, Choe CU, Siler DA, Arumugam TV, Orthey E, Gerloff C, Tolosa E, Magnus T (2009) Temporal and spatial dynamics of cerebral immune cell accumulation in stroke. Stroke. 40(5):1849-1857.

Gelderblom M, Weymar A, Bernreuther C, Velden J, Arunachalam P, Steinbach K, Orthey E, Arumugam TV, Leypoldt F, Simova O, Thom V, Friese MA, Prinz I, Holscher C, Glatzel M, Korn T, Gerloff C, Tolosa E, Magnus T (2012) Neutralization of the IL-17 axis diminishes neutrophil invasion and protects from ischemic stroke. Blood. 120(18):3793-3802.

Gene Ontology Consortium and Aleksander SA and Balhoff J and Carbon S and Cherry JM and Drabkin HJ and Ebert D and Feuermann M and Gaudet P and Harris NL and Hill DP and Lee R and Mi H and Moxon S and Mungall CJ and Muruganugan

A and Mushayahama T and Sternberg PW and Thomas PD and Van Auken K and Ramsey J and Siegele DA and Chisholm RL and Fey P and Aspromonte MC and Nugnes MV and Quaglia F and Tosatto S and Giglio M and Nadendla S and Antonazzo G and Attrill H and Dos Santos G and Marygold S and Strelets V and Tabone CJ and Thurmond J and Zhou P and Ahmed SH and Asanitthong P and Luna Buitrago D and Erdol MN and Gage MC and Ali Kadhum M and Li KYC and Long M and Michalak A and Pesala A and Pritazahra A and Saverimuttu SCC and Su R and Thurlow KE and Lovering RC and Logie C and Oliferenko S and Blake J and Christie K and Corbani L and Dolan ME and Drabkin HJ and Hill DP and Ni L and Sitnikov D and Smith C and Cuzick A and Seager J and Cooper L and Elser J and Jaiswal P and Gupta P and Jaiswal P and Naithani S and Lera-Ramirez M and Rutherford K and Wood V and De Pons JL and Dwinell MR and Hayman GT and Kaldunski ML and Kwitek AE and Laulederkind SJF and Tutaj MA and Vedi M and Wang SJ and D'Eustachio P and Aimo L and Axelsen K and Bridge A and Hyka-Nouspikel N and Morgat A and Aleksander SA and Cherry JM and Engel SR and Karra K and Miyasato SR and Nash RS and Skrzypek MS and Weng S and Wong ED and Bakker E, et al. (2023) The Gene Ontology knowledgebase in 2023. Genetics. 224(1).

Gil-Pulido J, Amezaga N, Jorgacevic I, Manthey HD, Rosch M, Brand T, Cidlinsky P, Schafer S, Beilhack A, Saliba AE, Lorenz K, Boon L, Prinz I, Waisman A, Korn T, Cochain C, Zernecke A (2022) Interleukin-23 receptor expressing gammadelta T cells locally promote early atherosclerotic lesion formation and plaque necrosis in mice. Cardiovasc Res. 118(14):2932-2945.

Goyal M, Demchuk AM, Menon BK, Eesa M, Rempel JL, Thornton J, Roy D, Jovin TG, Willinsky RA, Sapkota BL, Dowlatshahi D, Frei DF, Kamal NR, Montanera WJ, Poppe AY, Ryckborst KJ, Silver FL, Shuaib A, Tampieri D, Williams D, Bang OY, Baxter BW, Burns PA, Choe H, Heo JH, Holmstedt CA, Jankowitz B, Kelly M, Linares G, Mandzia JL, Shankar J, Sohn SI, Swartz RH, Barber PA, Coutts SB,

Smith EE, Morrish WF, Weill A, Subramaniam S, Mitha AP, Wong JH, Lowerison MW, Sajobi TT, Hill MD, Investigators ET (2015) Randomized assessment of rapid endovascular treatment of ischemic stroke. N Engl J Med. 372(11):1019-1030.

Hao Y, Hao S, Andersen-Nissen E, Mauck WM, 3rd, Zheng S, Butler A, Lee MJ, Wilk AJ, Darby C, Zager M, Hoffman P, Stoeckius M, Papalexi E, Mimitou EP, Jain J, Srivastava A, Stuart T, Fleming LM, Yeung B, Rogers AJ, McElrath JM, Blish CA, Gottardo R, Smibert P, Satija R (2021) Integrated analysis of multimodal single-cell data. Cell. 184(13):3573-3587 e3529.

He J, Fu F, Zhang W, Zhan Z, Cheng Z (2022) Prognostic significance of the clinical and radiological haemorrhagic transformation subtypes in acute ischaemic stroke: A systematic review and meta-analysis. Eur J Neurol. 29(11):3449-3459.

Herisson F, Frodermann V, Courties G, Rohde D, Sun Y, Vandoorne K, Wojtkiewicz GR, Masson GS, Vinegoni C, Kim J, Kim DE, Weissleder R, Swirski FK, Moskowitz MA, Nahrendorf M (2018) Direct vascular channels connect skull bone marrow and the brain surface enabling myeloid cell migration. Nat Neurosci. 21(9):1209-1217.

Jordao MJC, Sankowski R, Brendecke SM, Sagar, Locatelli G, Tai YH, Tay TL, Schramm E, Armbruster S, Hagemeyer N, Gross O, Mai D, Cicek O, Falk T, Kerschensteiner M, Grun D, Prinz M (2019) Single-cell profiling identifies myeloid cell subsets with distinct fates during neuroinflammation. Science. 363(6425).

Jovin TG, Chamorro A, Cobo E, de Miquel MA, Molina CA, Rovira A, San Roman L, Serena J, Abilleira S, Ribo M, Millan M, Urra X, Cardona P, Lopez-Cancio E, Tomasello A, Castano C, Blasco J, Aja L, Dorado L, Quesada H, Rubiera M, Hernandez-Perez M, Goyal M, Demchuk AM, von Kummer R, Gallofre M, Davalos A, Investigators RT (2015) Thrombectomy within 8 hours after symptom onset in ischemic stroke. N Engl J Med. 372(24):2296-2306.

Koh BI, Lee HJ, Kwak PA, Yang MJ, Kim JH, Kim HS, Koh GY, Kim I (2020) VEGFR2 signaling drives meningeal vascular regeneration upon head injury. Nat Commun. 11(1):3866.

Kolabas ZI, Kuemmerle LB, Perneczky R, Forstera B, Ulukaya S, Ali M, Kapoor S, Bartos LM, Buttner M, Caliskan OS, Rong Z, Mai H, Hoher L, Jeridi D, Molbay M, Khalin I, Deligiannis IK, Negwer M, Roberts K, Simats A, Carofiglio O, Todorov MI, Horvath I, Ozturk F, Hummel S, Biechele G, Zatcepin A, Unterrainer M, Gnorich J, Roodselaar J, Shrouder J, Khosravani P, Tast B, Richter L, Diaz-Marugan L, Kaltenecker D, Lux L, Chen Y, Zhao S, Rauchmann BS, Sterr M, Kunze I, Stanic K, Kan VWY, Besson-Girard S, Katzdobler S, Palleis C, Schadler J, Paetzold JC, Liebscher S, Hauser AE, Gokce O, Lickert H, Steinke H, Benakis C, Braun C, Martinez-Jimenez CP, Buerger K, Albert NL, Hoglinger G, Levin J, Haass C, Kopczak A, Dichgans M, Havla J, Kumpfel T, Kerschensteiner M, Schifferer M, Simons M, Liesz A, Krahmer N, Bayraktar OA, Franzmeier N, Plesnila N, Erener S, Puelles VG, Delbridge C, Bhatia HS, Hellal F, Elsner M, Bechmann I, Ondruschka B, Brendel M, Theis FJ, Erturk A (2023) Distinct molecular profiles of skull bone marrow in health and neurological disorders. Cell. 186(17):3706-3725 e3729.

Korsunsky I, Millard N, Fan J, Slowikowski K, Zhang F, Wei K, Baglaenko Y, Brenner M, Loh PR, Raychaudhuri S (2019) Fast, sensitive and accurate integration of single-cell data with Harmony. Nat Methods. 16(12):1289-1296.

Li H, Hu M, Huang Z, Wang Y, Xu Y, Deng J, Zhu M, Feng W, Xu X (2022) A single-cell atlas reveals the heterogeneity of meningeal immunity in a mouse model of Methyl CpG binding protein 2 deficiency. Front Immunol. 13:1056447.

Li Z, Antila S, Nurmi H, Chilov D, Korhonen EA, Fang S, Karaman S, Engelhardt B, Alitalo K (2023) Blockade of VEGFR3 signaling leads to functional impairment of dural lymphatic vessels without affecting autoimmune neuroinflammation. Sci Immunol. 8(82):eabq0375.

Louveau A, Smirnov I, Keyes TJ, Eccles JD, Rouhani SJ, Peske JD, Derecki NC, Castle D, Mandell JW, Lee KS, Harris TH, Kipnis J (2015) Structural and functional features of central nervous system lymphatic vessels. Nature. 523(7560):337-341.

Marsh S, Salmon M, Hoffman P (2023) samuel-marsh/scCustomize: Version 1.1.3 (v1.1.3). Zenodo.

Mazzitelli JA, Smyth LCD, Cross KA, Dykstra T, Sun J, Du S, Mamuladze T, Smirnov I, Rustenhoven J, Kipnis J (2022) Cerebrospinal fluid regulates skull bone marrow niches via direct access through dural channels. Nat Neurosci. 25(5):555-560.

McGinnis CS, Murrow LM, Gartner ZJ (2019) DoubletFinder: Doublet Detection in Single-Cell RNA Sequencing Data Using Artificial Nearest Neighbors. Cell Syst. 8(4):329-337 e324.

Moher D, Liberati A, Tetzlaff J, Altman DG, Group P (2009) Preferred reporting items for systematic reviews and meta-analyses: the PRISMA statement. BMJ. 339:b2535.

Mollgard K, Beinlich FRM, Kusk P, Miyakoshi LM, Delle C, Pla V, Hauglund NL, Esmail T, Rasmussen MK, Gomolka RS, Mori Y, Nedergaard M (2023) A mesothelium divides the subarachnoid space into functional compartments. Science. 379(6627):84-88.

Monaco G, Chen H, Poidinger M, Chen J, de Magalhaes JP, Larbi A (2016) flowAI: automatic and interactive anomaly discerning tools for flow cytometry data. Bioinformatics. 32(16):2473-2480.

Mrdjen D, Pavlovic A, Hartmann FJ, Schreiner B, Utz SG, Leung BP, Lelios I, Heppner FL, Kipnis J, Merkler D, Greter M, Becher B (2018) High-Dimensional Single-Cell Mapping of Central Nervous System Immune Cells Reveals Distinct Myeloid Subsets in Health, Aging, and Disease. Immunity. 48(2):380-395 e386.

Mundt S, Greter M, Becher B (2022) The CNS mononuclear phagocyte system in health and disease. Neuron. 110(21):3497-3512.

Munro DAD, Movahedi K, Priller J (2022) Macrophage compartmentalization in the

brain and cerebrospinal fluid system. Sci Immunol. 7(69):eabk0391.

Niu C, Yu J, Zou T, Lu Y, Deng L, Yun H, Si CY, Wu X, Jiang H, Guo T, Wu M, Kan T, Feng J, Yuan C, Yang X, Cheng Q, Dong J, Wang Q, Zhang J (2022) Identification of hematopoietic stem cells residing in the meninges of adult mice at steady state. Cell Rep. 41(6):111592.

Nogueira RG, Jadhav AP, Haussen DC, Bonafe A, Budzik RF, Bhuva P, Yavagal DR, Ribo M, Cognard C, Hanel RA, Sila CA, Hassan AE, Millan M, Levy EI, Mitchell P, Chen M, English JD, Shah QA, Silver FL, Pereira VM, Mehta BP, Baxter BW, Abraham MG, Cardona P, Veznedaroglu E, Hellinger FR, Feng L, Kirmani JF, Lopes DK, Jankowitz BT, Frankel MR, Costalat V, Vora NA, Yoo AJ, Malik AM, Furlan AJ, Rubiera M, Aghaebrahim A, Olivot JM, Tekle WG, Shields R, Graves T, Lewis RJ, Smith WS, Liebeskind DS, Saver JL, Jovin TG, Investigators DT (2018) Thrombectomy 6 to 24 Hours after Stroke with a Mismatch between Deficit and Infarct. N Engl J Med. 378(1):11-21.

Ogle D, Doll J, Wheeler A, Dinno A (2023) FSA: Simple Fisheries Stock Assessment Methods. R package version 0.9.5.

Pinho-Ribeiro FA, Deng L, Neel DV, Erdogan O, Basu H, Yang D, Choi S, Walker AJ, Carneiro-Nascimento S, He K, Wu G, Stevens B, Doran KS, Levy D, Chiu IM (2023) Bacteria hijack a meningeal neuroimmune axis to facilitate brain invasion. Nature. 615(7952):472-481.

Powers WJ, Rabinstein AA, Ackerson T, Adeoye OM, Bambakidis NC, Becker K, Biller J, Brown M, Demaerschalk BM, Hoh B, Jauch EC, Kidwell CS, Leslie-Mazwi TM, Ovbiagele B, Scott PA, Sheth KN, Southerland AM, Summers DV, Tirschwell DL (2019) Guidelines for the Early Management of Patients With Acute Ischemic Stroke: 2019 Update to the 2018 Guidelines for the Early Management of Acute Ischemic Stroke: A Guideline for Healthcare Professionals From the American Heart Association/American Stroke Association. Stroke. 50(12):e344-e418.

Pulous FE, Cruz-Hernandez JC, Yang C, Kaya Z, Paccalet A, Wojtkiewicz G, Capen D, Brown D, Wu JW, Schloss MJ, Vinegoni C, Richter D, Yamazoe M, Hulsmans M, Momin N, Grune J, Rohde D, McAlpine CS, Panizzi P, Weissleder R, Kim DE, Swirski FK, Lin CP, Moskowitz MA, Nahrendorf M (2022) Cerebrospinal fluid can exit into the skull bone marrow and instruct cranial hematopoiesis in mice with bacterial meningitis. Nat Neurosci. 25(5):567-576.

R Core Team R (2023) R: A language and environment for statistical computing.

Ratz M, von Berlin L, Larsson L, Martin M, Westholm JO, La Manno G, Lundeberg J, Frisen J (2022) Clonal relations in the mouse brain revealed by single-cell and spatial transcriptomics. Nat Neurosci. 25(3):285-294.

Rebejac J, Eme-Scolan E, Arnaud Paroutaud L, Kharbouche S, Teleman M, Spinelli L, Gallo E, Roussel-Queval A, Zarubica A, Sansoni A, Bardin Q, Hoest P, Michallet MC, Brousse C, Crozat K, Manglani M, Liu Z, Ginhoux F, McGavern DB, Dalod M, Malissen B, Lawrence T, Rua R (2022) Meningeal macrophages protect against viral neuroinfection. Immunity. 55(11):2103-2117 e2110.

Ribeiro M, Brigas HC, Temido-Ferreira M, Pousinha PA, Regen T, Santa C, Coelho JE, Marques-Morgado I, Valente CA, Omenetti S, Stockinger B, Waisman A, Manadas B, Lopes LV, Silva-Santos B, Ribot JC (2019) Meningeal gammadelta T cell-derived IL-17 controls synaptic plasticity and short-term memory. Sci Immunol. 4(40).

Ribot JC, Lopes N, Silva-Santos B (2021) gammadelta T cells in tissue physiology and surveillance. Nat Rev Immunol. 21(4):221-232.

Rustenhoven J, Drieu A, Mamuladze T, de Lima KA, Dykstra T, Wall M, Papadopoulos Z, Kanamori M, Salvador AF, Baker W, Lemieux M, Da Mesquita S, Cugurra A, Fitzpatrick J, Sviben S, Kossina R, Bayguinov P, Townsend RR, Zhang Q, Erdmann-Gilmore P, Smirnov I, Lopes MB, Herz J, Kipnis J (2021) Functional characterization of the dural sinuses as a neuroimmune interface. Cell. 184(4):1000-1016 e1027.

Sandrock I, Reinhardt A, Ravens S, Binz C, Wilharm A, Martins J, Oberdorfer L, Tan L, Lienenklaus S, Zhang B, Naumann R, Zhuang Y, Krueger A, Forster R, Prinz I (2018) Genetic models reveal origin, persistence and non-redundant functions of IL-17-producing gammadelta T cells. J Exp Med. 215(12):3006-3018.

Saver JL, Goyal M, Bonafe A, Diener HC, Levy EI, Pereira VM, Albers GW, Cognard C, Cohen DJ, Hacke W, Jansen O, Jovin TG, Mattle HP, Nogueira RG, Siddiqui AH, Yavagal DR, Baxter BW, Devlin TG, Lopes DK, Reddy VK, du Mesnil de Rochemont R, Singer OC, Jahan R, Investigators SP (2015) Stent-retriever thrombectomy after intravenous t-PA vs. t-PA alone in stroke. N Engl J Med. 372(24):2285-2295.

Schafflick D, Wolbert J, Heming M, Thomas C, Hartlehnert M, Borsch AL, Ricci A, Martin-Salamanca S, Li X, Lu IN, Pawlak M, Minnerup J, Strecker JK, Seidenbecher T, Meuth SG, Hidalgo A, Liesz A, Wiendl H, Meyer Zu Horste G (2021) Single-cell profiling of CNS border compartment leukocytes reveals that B cells and their progenitors reside in non-diseased meninges. Nat Neurosci. 24(9):1225-1234.

Scheyltjens I, Van Hove H, De Vlaminck K, Kancheva D, Bastos J, Vara-Perez M, Pombo Antunes AR, Martens L, Scott CL, Van Ginderachter JA, Saeys Y, Guilliams M, Vandamme N, Movahedi K (2022) Single-cell RNA and protein profiling of immune cells from the mouse brain and its border tissues. Nat Protoc. 17(10):2354-2388.

Schnizlein-Bick CT, Spritzler J, Wilkening CL, Nicholson JK, O'Gorman MR (2000) Evaluation of TruCount absolute-count tubes for determining CD4 and CD8 cell numbers in human immunodeficiency virus-positive adults. Site Investigators and The NIAID DAIDS New Technologies Evaluation Group. Clin Diagn Lab Immunol. 7(3):336-343.

Shichita T, Ito M, Morita R, Komai K, Noguchi Y, Ooboshi H, Koshida R, Takahashi S, Kodama T, Yoshimura A (2017) MAFB prevents excess inflammation after

ischemic stroke by accelerating clearance of damage signals through MSR1. Nat Med. 23(6):723-732.

Shichita T, Sugiyama Y, Ooboshi H, Sugimori H, Nakagawa R, Takada I, Iwaki T, Okada Y, Iida M, Cua DJ, Iwakura Y, Yoshimura A (2009) Pivotal role of cerebral interleukin-17-producing gammadeltaT cells in the delayed phase of ischemic brain injury. Nat Med. 15(8):946-950.

Su X, Yang S, Li Y, Xiang Z, Tao Q, Liu S, Yin Z, Zhong L, Lv X, Zhou L (2023) gammadelta T cells recruitment and local proliferation in brain parenchyma benefit anti-neuroinflammation after cerebral microbleeds. Front Immunol. 14:1139601.

Subramanian A, Tamayo P, Mootha VK, Mukherjee S, Ebert BL, Gillette MA, Paulovich A, Pomeroy SL, Golub TR, Lander ES, Mesirov JP (2005) Gene set enrichment analysis: a knowledge-based approach for interpreting genome-wide expression profiles. Proc Natl Acad Sci U S A. 102(43):15545-15550.

Tan L, Sandrock I, Odak I, Aizenbud Y, Wilharm A, Barros-Martins J, Tabib Y, Borchers A, Amado T, Gangoda L, Herold MJ, Schmidt-Supprian M, Kisielow J, Silva-Santos B, Koenecke C, Hovav AH, Krebs C, Prinz I, Ravens S (2019) Single-Cell Transcriptomics Identifies the Adaptation of Scart1(+) Vgamma6(+) T Cells to Skin Residency as Activated Effector Cells. Cell Rep. 27(12):3657-3671 e3654.

Tirosh I, Izar B, Prakadan SM, Wadsworth MH, 2nd, Treacy D, Trombetta JJ, Rotem A, Rodman C, Lian C, Murphy G, Fallahi-Sichani M, Dutton-Regester K, Lin JR, Cohen O, Shah P, Lu D, Genshaft AS, Hughes TK, Ziegler CG, Kazer SW, Gaillard A, Kolb KE, Villani AC, Johannessen CM, Andreev AY, Van Allen EM, Bertagnolli M, Sorger PK, Sullivan RJ, Flaherty KT, Frederick DT, Jane-Valbuena J, Yoon CH, Rozenblatt-Rosen O, Shalek AK, Regev A, Garraway LA (2016) Dissecting the multicellular ecosystem of metastatic melanoma by single-cell RNA-seq. Science. 352(6282):189-196.

van den Brink SC, Sage F, Vertesy A, Spanjaard B, Peterson-Maduro J, Baron CS, Robin

C, van Oudenaarden A (2017) Single-cell sequencing reveals dissociation-induced gene expression in tissue subpopulations. Nat Methods. 14(10):935-936.

Van Hove H, Martens L, Scheyltjens I, De Vlaminck K, Pombo Antunes AR, De Prijck S, Vandamme N, De Schepper S, Van Isterdael G, Scott CL, Aerts J, Berx G, Boeckxstaens GE, Vandenbroucke RE, Vereecke L, Moechars D, Guilliams M, Van Ginderachter JA, Saeys Y, Movahedi K (2019) A single-cell atlas of mouse brain macrophages reveals unique transcriptional identities shaped by ontogeny and tissue environment. Nat Neurosci. 22(6):1021-1035.

Wang W, Jiang B, Sun H, Ru X, Sun D, Wang L, Wang L, Jiang Y, Li Y, Wang Y, Chen Z, Wu S, Zhang Y, Wang D, Wang Y, Feigin VL, Investigators NE-C (2017) Prevalence, Incidence, and Mortality of Stroke in China: Results from a Nationwide Population-Based Survey of 480 687 Adults. Circulation. 135(8):759-771.

Wang Y, Li S, Pan Y, Li H, Parsons MW, Campbell BCV, Schwamm LH, Fisher M, Che F, Dai H, Li D, Li R, Wang J, Wang Y, Zhao X, Li Z, Zheng H, Xiong Y, Meng X, Investigators T- (2023) Tenecteplase versus alteplase in acute ischaemic cerebrovascular events (TRACE-2): a phase 3, multicentre, open-label, randomised controlled, non-inferiority trial. Lancet. 401(10377):645-654.

Wu T, Hu E, Xu S, Chen M, Guo P, Dai Z, Feng T, Zhou L, Tang W, Zhan L, Fu X, Liu S, Bo X, Yu G (2021) clusterProfiler 4.0: A universal enrichment tool for interpreting omics data. Innovation (Camb). 2(3):100141.

Xue R, Zhang Q, Cao Q, Kong R, Xiang X, Liu H, Feng M, Wang F, Cheng J, Li Z, Zhan Q, Deng M, Zhu J, Zhang Z, Zhang N (2022) Liver tumour immune microenvironment subtypes and neutrophil heterogeneity. Nature. 612(7938):141-147.

Yang S, Corbett SE, Koga Y, Wang Z, Johnson WE, Yajima M, Campbell JD (2020) Decontamination of ambient RNA in single-cell RNA-seq with DecontX. Genome Biol. 21(1):57.

Yeo LLL, Bhogal P, Gopinathan A, Cunli Y, Tan B, Andersson T (2019) Why Does Mechanical Thrombectomy in Large Vessel Occlusion Sometimes Fail? : A Review of the Literature. Clin Neuroradiol. 29(3):401-414.

Zhang J (2022) GseaVis: An Implement R Package to Visualize GSEA Results.

Zilionis R, Engblom C, Pfirschke C, Savova V, Zemmour D, Saatcioglu HD, Krishnan I, Maroni G, Meyerovitz CV, Kerwin CM, Choi S, Richards WG, De Rienzo A, Tenen DG, Bueno R, Levantini E, Pittet MJ, Klein AM (2019) Single-Cell Transcriptomics of Human and Mouse Lung Cancers Reveals Conserved Myeloid Populations across Individuals and Species. Immunity. 50(5):1317-1334 e1310.

8. Acknowledgments

A two-year journey in the Experimental Research in Stroke and Inflammation (ERSI) lab is coming to an end, I have many unforgettable memories within these two years. Finally, I am going to finish this part of my life stage. And I am ready to open a new chapter.

Many thanks to my dear wife, Shuo Liu. Her love and care helped me overcome all sorts of problems. Every day I stay with her is the best day I want. Thanks to my parents and little sister, family is always the harbor for me and is the softest place in my heart. I love them and their love makes me stronger.

Many thanks to PD Dr. Mathias Gelderblom and Prof. Tim Magnus for giving me the invitation letter, so that I can apply for the visa and learn abroad. Their supports enable me to explore the scientific questions. Mathias is very patient and helpful, he gives me so much feedback regarding the thesis, and I am very grateful for his help.

Thanks to the China Scholarship Council a lot for sponsorship. This precious 2-year funding enables me to learn and experience without worrying about living.

Haodi Cai, Jiani Jiang, and Dr. Yuqi Gui supported me a lot during these two years. Especially Haodi, we have experienced too many things together. We help each other and share the happiness and sorrow. Hind Haj Ahmad, Javier Randez, Mamta Panda, and PhD. Santra Brenna are very friendly persons. I enjoy the days of working with colleagues. Although I can't stay longer here, memories are valuable enough.

Karolin Gustmann helps me a lot with stroke modeling and mice line management, and I also appreciate the help I get from Jasmin Pabla, Lennart Pöls, and Tobias Großhauser. They are very important supporters in this lab.

Thanks to Dr. Alina Jander for introducing me to meninges-related experiments and knowledge in the very beginning. Thanks to Dr. Justine Muensterberg for giving me a 400-euro extra income every month as a bonus for emergency duties I take. And the guidance she gave to me in the very beginning. Besides, I could not live next to UKE in the first year without her help.

Thanks to other tutors and students in the lab for all the help that ever gave to me.

I believe ERSI will be a better scientific organization in the future, and I believe ERSI can publish more highly influenced papers.

I will keep the knowledge and beautiful moments in my mind, and prepare for the next chapter of my life.

9. Resume

Lebenslauf entfällt aus datenschutzrechtlichen Gründen.

10. Eidesstattliche Versicherung

Ich versichere ausdrücklich, dass ich die Arbeit selbständig und ohne fremde Hilfe verfasst, andere als die von mir angegebenen Quellen und Hilfsmittel nicht benutzt und die aus den benutzten Werken wörtlich oder inhaltlich entnommenen Stellen einzeln nach Ausgabe (Auflage und Jahr des Erscheinens), Band und Seite des benutzten Werkes kenntlich gemacht habe.
Ferner versichere ich, dass ich die Dissertation bisher nicht einem Fachvertreter an einer anderen Hochschule zur Überprüfung vorgelegt oder mich anderweitig um Zulassung zur Promotion beworben habe.
Ich erkläre mich einverstanden, dass meine Dissertation vom Dekanat der Medizinischen Fakultät mit einer gängigen Software zur Erkennung von Plagiaten überprüft werden kann.

Unterschrift: .....